

Academic Dissertation

**Optimizing a Calorimetry Chamber for
the RF Characterization of
Superconductors**

Keckert, Sebastian (Universität Siegen)

01 July 2015



The EuCARD-2 Enhanced European Coordination for Accelerator Research & Development project is co-funded by the partners and the European Commission under Capacities 7th Framework Programme, Grant Agreement 312453.

This work is part of EuCARD-2 Work Package **12: Innovative Radio Frequency Technologies (RF)**.

The electronic version of this EuCARD-2 Publication is available via the EuCARD-2 web site <http://eucard2.web.cern.ch/> or on the CERN Document Server at the following URL:
<<http://cds.cern.ch/search?p=CERN-THESIS-2015-339>>

OPTIMIZING A CALORIMETRY CHAMBER FOR THE RF CHARACTERIZATION OF SUPERCONDUCTORS

Masterarbeit

zur Erlangung des akademischen Grades

Master of Science

(M. Sc.)

der Universität Siegen



Department Physik

vorgelegt von

Sebastian Keckert

Juli 2015

Contents

1	Introduction	1
2	Theory	3
2.1	Basics of RF Superconductivity	3
2.2	Surface Resistance	4
2.3	Superconducting Thin Films	8
3	The Quadrupole Resonator	11
3.1	RF Design	11
3.2	Surface Resistance Measurement	13
3.3	Measuring Penetration Depth and Further Properties	16
4	Simulations	19
4.1	Introduction	19
4.2	Theory and Analytical Considerations	20
4.2.1	Radial Deviations	20
4.2.2	Magnetic Field Enhancement	21
4.3	Software	24
4.4	Geometry	24
4.5	Step 1: Circumferential Gap	26
4.5.1	Results of the Baseline Geometry	27
4.5.2	Results from Simulation Geometry Variations	30
4.6	Step 2: Separated Gaps	32
5	Construction and Test of a Prototype Chamber	35
5.1	Results from Simulations and Design Requirements	35
5.1.1	Vacuum and Cleanliness	35
5.1.2	Thermal Conductivity	35
5.2	Description of the Design	36
5.2.1	Sample Holder	36
5.2.2	Tube and Bottom Flange	37
5.3	Vacuum Tests	39
5.3.1	First Tests without Additional Gasket	39
5.3.2	Measurements with Indium Gasket	40

6	Design and Production of the Niobium Chamber	41
6.1	Design Changes due to Aluminum Prototype Tests	41
6.1.1	Implementation of an Indium Wire Gasket	41
6.1.2	Modification of the Bolting	42
6.1.3	Geometric Dimensioning and Tolerancing	43
6.2	Production and Surface Treatment	43
6.3	Leak Rate Measurements	44
6.3.1	Measurements at Room Temperature	44
6.3.2	Thermal Cycles and Tests at Cryogenic Temperatures	45
7	First RF Measurements	47
7.1	Measurement Setup	47
7.1.1	Resonant Frequency and Height of Calorimetry Chamber	47
7.2	Superconducting Properties	48
7.2.1	Surface Resistance	48
7.2.2	Penetration Depth and RRR	51
7.3	Thermal Properties	53
7.3.1	Temperature Profiles	53
7.3.2	Thermal Conductivity	55
7.4	Further Surface Investigation	57
7.4.1	Profilometry	57
7.4.2	Chemical Composition Analysis	59
8	Summary and Outlook	61
8.1	Design of an Optimized Calorimetry Chamber	61
8.2	First RF Measurement	62
8.3	Outlook	62
A	Appendix	i
A.1	Picture of the Vacuum Test Environment	i
A.2	Pictures of Sample and Assembled Calorimetry Chamber	ii
	Bibliography	iii

1 Introduction

Within the last decades, particle accelerators became the key tool for a wide range of most diverse applications. Both accelerated particles and the radiation created from it is used for investigating fundamental questions of matter, complex medical treatments, safety technologies and industrial production processes. The demands on the accelerated particle beams are as varied as their applications.

Many applications call for continuous operation at high accelerating gradient, which can only be achieved using superconducting radio frequency (SRF) systems. The key feature of superconducting cavities is given by their surface resistance R_S , which is at microwave frequencies used for acceleration 5-6 orders of magnitude smaller than the one of copper.

Currently, SRF cavities are made out of niobium. Niobium has the highest superconducting transition temperature T_c of all elements and shows best RF properties. Furthermore, optimized production procedures are available. Modern niobium cavities perform close to the theoretical limit. In order to push for higher accelerating gradients as well as for lower total power consumption, new materials are needed.

Operating superconducting cavities, an optimum temperature in terms of total power consumption has to be identified. RF dissipation decreases towards lower temperatures, while the refrigeration power required from the cryoplant is increasing due to the Carnot efficiency. For niobium at frequencies above 500 MHz, temperatures of 1.8 K to 2.0 K are used commonly, yielding an overall cryogenic efficiency of only 1 %. Finding new materials with higher T_c would allow operation at higher temperature, which significantly reduces the cryoplant requirements.

For the availability of higher accelerating gradients, materials with higher values of critical magnetic field are needed.

Developing SRF cavities beyond the theoretical limits of niobium, promising research is ongoing investigating superconducting thin films. By using superconducting coatings, several new concepts are introduced: The mechanical and thermal properties of the cavity are carried by the substrate and do not restrict the choice of superconductor any longer. Furthermore, multilayer structures become possible, which provide the potential to exceed the field limitation of a bulk material.

For systematic research on superconductors, precision measurements of the RF properties as a function of applied magnetic field, operating temperature and frequency are required. The exploration of the full parameter space is difficult to perform with standard SRF cavities. For the purpose of characterizing planar circular samples the Quadrupole Resonator (QPR) was

developed at CERN. The samples for the QPR can be both coatings, on a substrate as well as solid superconductors. Currently the QPR has a complex sample system which is too big for typical coating systems. If flat samples are to be characterized, electron beam welding of the sample to the calorimetric system is required.

In this thesis an optimized calorimetry chamber is developed, providing flat and easy mountable samples. Furthermore, it enables exchangeability of samples between the resonators at HZB and CERN.

The thesis is structured as follows: First, a short introduction into SRF is given. The focus is on the surface resistance and a theoretical derivation is given using the two-fluid model of superconductivity. Subsequently, the Quadrupole Resonator is introduced. The RF design is presented and the calorimetric measurement principle, enabling precision measurements of the RF surface resistance, is derived. In chapter 4 the impact of a demountable sample on the RF inside the resonator is investigated and boundary conditions concerning the technical realization are extracted. Afterwards, a prototype made out of aluminum is studied (chapter 5) and the experience gained there is used to define a final design (chapter 6). The new design could already be used for a first measurement at CERN with the results given in chapter 7.

At the end of the thesis a summary of the obtained results is given. Observed difficulties are discussed together with an outlook towards possible future steps using the optimized calorimetry chamber.

2 Theory

Superconductivity was observed first by Heike Kamerlingh Onnes in 1911. While measuring the electrical resistance of mercury in a bath of liquid helium, he noticed a jump at 4.2 K towards an unquantifiably small resistance [1,2]. At that time an electrical resistance vanishing at low temperatures was predicted by some theories, but further investigations on the sharp transition indicated something new [3]. Few years later Kamerlingh Onnes built the first superconducting coil and he was able to prove the existence of persistent currents in a closed superconducting circuit [4,5].

The theoretical explanation of superconductivity took quite some time. In 1935 Fritz and Heinz London provided a first, phenomenological explanation [6]. 15 years later Ginzburg and Landau formulated a thermodynamic description [7]. Now the existence of non-uniform effects like the mixed state in type II superconductors could be explained. In 1957 with the work of Bardeen, Schrieffer and Cooper a microscopic theory of superconductivity became available [8,9]. One year later Mattis and Bardeen provided an explanation for electric losses in the presence of oscillating electromagnetic fields [10]. This is especially important for the application of superconductivity to radio-frequency cavities.

In this chapter some theoretical aspects of RF superconductivity (SRF) are presented. The focus is on the surface resistance, denoting a key figure of superconducting cavities and which can be measured precisely using the Quadrupole Resonator (QPR). It is introduced in chapter 3.

2.1 Basics of RF Superconductivity

In general an accelerating cavity can be described by an equivalent parallel RLC circuit. The resonant frequency ω and the quality factor Q of this circuit are given by

$$\omega = \frac{1}{\sqrt{LC}} \quad (2.1)$$

$$Q = \frac{\omega U}{P_{\text{diss}}} = \frac{R}{\sqrt{L/C}} \quad (2.2)$$

with the stored energy U and the dissipated power P_{diss} . Using the circuit definition, the accelerating voltage V is related to the dissipated power as follows [11]:

$$P_{\text{diss}} = \frac{V^2}{2R} \quad (2.3)$$

RF dissipation occurs due to Joule heating by the magnetic field \vec{H} at the cavity walls

$$\frac{dP}{dS} = \frac{1}{2}R_S|\vec{H}|^2. \quad (2.4)$$

R_S denotes the surface resistance, a more detailed discussion on the RF surface resistance is given in sec 2.2. In order to obtain the total power dissipated inside a cavity, eq. 2.4 has to be integrated over its interior surface. Assuming R_S to be uniform on the entire surface, yields for the quality factor (eq. 2.2)

$$Q = \frac{2\omega U}{R_S \int_S |\vec{H}|^2 dS} = \frac{G}{R_S}. \quad (2.5)$$

For real cavities the stored energy U and the surface integral as stated above cannot be calculated analytically. The geometry factor G is introduced to relate the surface resistance to the quality factor. G is determined from numerical simulations and depends only on the electromagnetic field configuration and therefore on the shape but not on the size of the cavity [12]. With the help of the geometry factor eq. 2.3 can be rewritten to

$$P_{\text{diss}} = \frac{R_S V^2}{2G(R/Q)} \quad (2.6)$$

introducing the normalized shunt impedance R/Q . This figure of merit describes the power dissipated by the cavity walls independent of the choice of material. Common values for R/Q range from $50\,\Omega$ for superconducting cavities up to few hundred Ω for normal conducting structures [11]. Since typical values of optimized geometry factors for accelerating cavities are in the range of $250\,\Omega$ [13], eq. 2.6 indicates a strong point of superconducting cavities: If operated continuously (cw), the dissipated power for normal conducting cavities becomes unfeasibly high for gradients of few MV/m. Thanks to superconductivity the surface resistance is reduced by about six orders of magnitude enabling cw operation of cavities at these gradients, even justifying the effort of operating at cryogenic temperatures which diminishes this benefit by only three orders of magnitude.

2.2 Surface Resistance

The existence of the RF surface resistance of superconductors, despite the absence of DC dissipation, can be explained by the two-fluid model. This model was introduced first by C. J. Gorter and H. Casimir and assumes two fluids of charge carriers composing the conductivity of a superconductor [14, 15]. Below the critical temperature T_c an increasing fraction of electrons is bound together building Cooper pairs, due to an attraction mediated by the material's lattice. These pairs, constituting the superfluid component, move without friction but have inertia. For static currents the inertia of Cooper pairs does not matter and the superfluid charge carriers constitute a “short circuit”, leading to zero DC resistance of a superconductor. With increasing frequency,

a growing fraction of current is mediated by the remaining unbound electrons (normal fluid component), causing resistive losses as in the normal conducting state. Note that the concept of bound electrons (Cooper pairs) requires fermion spin statistic and was discovered much later by L. N. Cooper [16]. Below, a derivation of the surface resistance in the two-fluid model is given, starting from the London equations. The calculation of the London penetration depth follows [12] and [17]. Afterwards the surface resistance is derived according to [18], using the penetration depth obtained before.

The London theory is based on two fundamental equations which were assumed phenomenologically. The first London equation describes the superconducting current density as for a perfect conductor:

$$\frac{\partial \vec{j}_s}{\partial t} = \frac{n_s e^2}{m} \vec{E} \quad (2.7)$$

n_s denotes the superfluid density, satisfying $n_s + n_n = n$ with normal fluid density n_n and total electron density n . This equation comes out of the Newton equation for a current density $\vec{j}_s = -n_s e \vec{v}$ in case of free acceleration by an external electric field \vec{E} . Plugging eq. 2.7 into Faraday's law $\nabla \times \vec{E} = -\partial \vec{B} / \partial t$ yields

$$\frac{\partial}{\partial t} \left(\nabla \times \vec{j}_s + \frac{n_s e^2}{m} \vec{B} \right) = 0. \quad (2.8)$$

At the time of the London theory, the Meissner effect, characterized by the complete expulsion of magnetic flux by a superconductor, was already known. London realized that in order to explain this effect one further assumption is needed. In contrast to superconductors, a perfect conductor does not show flux expulsion under all conditions. As described by eq. 2.8 a magnetic field independent of time may exist in a perfect conductor. London required the quantity in eq. 2.8 to be not only constant but also equal to zero. This results in the second London equation

$$\nabla \times \vec{j}_s = -\frac{n_s e^2}{m} \vec{B}. \quad (2.9)$$

Taking the curl of Ampere's law $\nabla \times \vec{B} = \mu_0 \vec{j}$ and using $\nabla \times \nabla \times \vec{B} = -\nabla^2 \vec{B}$ yields

$$\nabla^2 \vec{B} = -\mu_0 \nabla \times \vec{j}_s = \frac{\mu_0 n_s e^2}{m} \vec{B} = \frac{1}{\lambda_L^2} \vec{B}. \quad (2.10)$$

Here the London penetration depth $\lambda_L = \sqrt{\frac{m}{\mu_0 n_s e^2}}$ is introduced. Later, we will see that λ_L acts similar to the skin depth known from the normal conducting case. Note that the penetration depth depends on n_s which increases from zero at T_c up to its maximum value at $T = 0$ K. In the two-fluid model of Gorter and Casimir the superfluid electron density is given by [17]

$$\frac{n_s(T)}{n} = 1 - \left(\frac{T}{T_c} \right)^4 \quad (2.11)$$

2.2 Surface Resistance

yielding the temperature dependence of λ_L :

$$\lambda_L(T) = \frac{\lambda_L(0)}{\sqrt{1 - \left(\frac{T}{T_c}\right)^4}} \quad (2.12)$$

The normal fluid current density is given by $\vec{j}_n = \sigma_n \vec{E}$ as for a normal conductor. Considering the surface resistance in case of an RF field, the superfluid current density is assumed to be $\vec{j}_s = \vec{j}_{s0} e^{i\omega t}$. With $\partial \vec{j}_s / \partial t = i\omega \vec{j}_s$ the first London equation (2.7) yields

$$\vec{j}_s = \frac{-i}{\omega \mu_0 \lambda_L^2} \vec{E} = -i \frac{n_s e^2}{m \omega} \vec{E} = -i \sigma_s \vec{E} \quad (2.13)$$

with the superfluid conductivity

$$\sigma_s = \frac{n_s e^2}{m \omega} = \frac{1}{\omega \mu_0 \lambda_L^2}. \quad (2.14)$$

The total current density results to $\vec{j} = \vec{j}_n + \vec{j}_s = (\sigma_n - i\sigma_s) \vec{E}$. Now, a surface at $x = 0$ is considered. In case of a normal conductor the (parallel) magnetic field penetrating the material decays exponentially, characterized by the skin depth

$$\delta = \sqrt{\frac{2}{\omega \mu_0 \sigma}}. \quad (2.15)$$

Using Ampere's law, the following relation between electric and magnetic field is obtained [18]:

$$E_z(x, t) = -\frac{1+i}{\sigma \delta} H_y(x, t) \quad (2.16)$$

The complex surface impedance is defined as

$$Z_S = \frac{|E_{||}|}{|H_{||}|} = R_S + iX_S = \frac{|E_z(x=0)|}{|H_y(x=0)|} = \frac{1+i}{\sigma \delta} \quad (2.17)$$

with surface resistance R_S and surface reactance X_S [18]. For the two-fluid model the conductivity σ is replaced by $\sigma_n - i\sigma_s$. By using $(1+x)^{-1/2} \approx 1 - x/2$ with $x = i\sigma_n/\sigma_s$ the skin depth can be rewritten as

$$\delta = \sqrt{\frac{2}{\omega \mu_0 (\sigma_n - i\sigma_s)}} \approx (1+i) \lambda_L \left(1 - i \frac{\sigma_n}{2\sigma_s}\right). \quad (2.18)$$

At temperatures $T \ll T_c$ the approximation $\sigma_n \ll \sigma_s$ is valid and δ is given by the London penetration depth. Plugged into eq. 2.17 results to

$$Z_S = \frac{1}{\lambda_L} \cdot \frac{1}{(\sigma_n - i\sigma_s) \left(1 - i \frac{\sigma_n}{2\sigma_s}\right)}. \quad (2.19)$$

Neglecting all terms of order σ_n^2 yields

$$Z_S = \frac{1}{2}\sigma_n\mu_0^2\omega^2\lambda_L^3 + i\omega\mu_0\lambda_L \quad (2.20)$$

with the surface resistance

$$R_S = \frac{1}{2}\sigma_n\mu_0^2\omega^2\lambda_L^3. \quad (2.21)$$

This formula indicates that material with high resistance in the normal state will show less losses when superconducting. The impact of this behavior on superconducting cavities and the attractiveness of cavities coated with thin films is discussed later (see sec. 2.3).

Regarding the total power dissipation of an accelerator system, the power dissipated in one cell (eq. 2.6) has to be multiplied by the number of cells. Expressing the accelerating voltage by total energy and number of cells ($V = E/N$), leads to the dependence on frequency

$$P_{\text{tot}} = N \cdot P_{\text{diss}} \propto \frac{E^2}{N} R_S \propto \frac{R_S}{L_{\text{tot}} \omega} \quad (2.22)$$

with cavity frequency ω and the total length of the accelerator L_{tot} [19]. For normal conducting cavities the surface resistance increases slowly with frequency: $R_S \propto \omega^{1/2}$ (see eq. 2.15). Plugged into eq. 2.22 yields $P_{\text{tot,nc}} \propto \omega^{-1/2}$, while for superconducting systems low frequencies are preferred due to the quadratic rise of surface resistance with frequency: $P_{\text{tot,sc}} \propto \omega$.

The temperature dependence of R_S is given by σ_n and hence by the number of normal conducting electrons: $R_S \propto \sigma_n \propto n_n$. Due to the thermal breakup of Cooper pairs with increasing temperature, a good approximation for $T < T_c/2$ is given by the exponential behavior

$$R_S \propto \exp\left(-\frac{\Delta}{k_B T}\right) \quad (2.23)$$

with the superconducting energy gap Δ [18]. The energy gap is directly proportional to the critical temperature [17], hence a lower value of surface resistance is expected for materials with higher T_c .

With the very successful BCS theory, discovered in 1957, a microscopic explanation of superconductivity became available. Introducing the coherence length ξ_0 , the spacial scale of the transition from normal conducting to superconducting is described. Furthermore ξ_0 denotes the size of a Cooper pair, i.e. the distance between two bound electrons. Comparing λ_L and ξ_0 results in the separation condition for superconductors of Type I and II. For a Ginzburg-Landau parameter

$$\kappa_{\text{GL}} = \frac{\lambda_L}{\xi_0} \quad (2.24)$$

smaller than $1/\sqrt{2}$ the superconductor exhibits the Meissner effect if $T < T_c$ and $H < H_c$, otherwise superconductivity breaks down. These materials are called Type I. In case of $\kappa_{\text{GL}} > 1/\sqrt{2}$ the surface energy between a superconducting and normal conducting region becomes nega-

2.3 Superconducting Thin Films

tive, i. e. the total energy is lowered by forming superconducting/normal conducting boundaries. These Type II superconductors show regular patterns of quantized magnetic flux vortices penetrating the bulk, for magnetic fields above a certain threshold (H_{c1}). Vortices contain a normal conducting core which moves due to a Lorentz force by the applied RF magnetic field, causing additional losses. Therefore, superconducting cavities have to be operated at fields without vortex penetration. Further investigations of the phase transition from superconducting to normal conducting yield the existence of a superheated state. Up to a field $H_{sh} > H_{c1}$ the Meissner state can exist metastably without vortex penetration. This field, which is independent of the upper critical field H_{c2} , defines the ultimate RF limitation of a superconductor [12].

In the framework of BCS an analytical expression for the surface resistance is available only under certain assumptions. For niobium under the conditions of this thesis a simplified expression is given by

$$R_{BCS}(f, T) [\Omega] \approx 2 \cdot 10^{-4} \frac{K}{(GHz)^2} \left(\frac{f}{1.5} \right)^2 \frac{1}{T} \exp \left(-\frac{17.67 K}{T} \right) \quad (2.25)$$

which is valid for $T < T_c/2$ and $\omega \ll 2\Delta/h \approx 10^{12}$ Hz. The dependence of R_S on the conductivity in the normal state is neglected in this formula [12].

Measurements with SRF cavities showed a superposition of BCS surface resistance with an additional contribution independent of temperature:

$$R_S = R_{BCS} + R_{res}. \quad (2.26)$$

The residual resistance R_{res} especially limits the surface resistance at low temperature and low frequency, where the BCS contribution is small. R_{res} is related to several mechanisms, like surface impurities, defects or trapped magnetic flux [12]. At HZB research is currently ongoing investigating the influence of magnetic flux trapped due to cool-down conditions [20–22].

2.3 Superconducting Thin Films

In order to characterize the purity of a (metallic) superconductor, the Residual Resistivity Ratio (RRR) is introduced. It describes the ratio of electrical resistivity at room temperature, compared to the resistivity at liquid helium temperature in the normal conducting state [12].

$$RRR = \frac{\rho(300 K)}{\rho(4.2 K)} = \frac{\sigma(4.2 K)}{\sigma(300 K)} \quad (2.27)$$

The RRR is linked directly to the thermal conductivity (k_s) in the superconducting state at 4.2 K. Empirically, one finds for niobium that [12]

$$k_s \left[\frac{W}{m \cdot K} \right] = \frac{RRR}{4}. \quad (2.28)$$

Recall the dependence of the surface resistance, obtained from the two-fluid model: Increasing normal state resistivity, i.e. a lower RRR, yields smaller R_S . The full calculation using BCS theory shows similarly increasing surface resistance with RRR. One important difference occurs at low RRR. Following BCS, minimum R_S is reached for RRR between 10 and 20. At this point the electron mean free path becomes smaller than the BCS coherence length and the fields and currents inside the superconductor vary significantly within ξ_0 . In this case non-local effects become important and the first London equation breaks down, resulting in a deviation from $R_S \propto \sigma_n$. Lower values of RRR causes the resistance to increase again [12]. This raises an issue for superconducting cavities: Cooled by a liquid helium bath, all heat produced on the interior surface has to be transported through the bulk quickly. Otherwise warming the inner wall of the cavity will increase the surface resistance, which in turn leads to growing power dissipation. This thermal instability is referred to as thermal runaway. The reason of a thermal runaway can be both “normal” warming due to the superconducting surface resistance as well as surface defects (e.g. normal conducting impurities or particles) causing additional RF dissipation. Present cavities use niobium of RRR 300 in order to overcome this field limitation.

A very promising and already used technique to resolve this issue is coating a thin film on a copper substrate. With a thickness of few μm ($\lambda_L \approx 40\text{ nm}$), only the superconductor is “seen” by the RF. Now a film of low RRR can be used, while heat transfer and mechanical stability is carried by the substrate. Nevertheless this approach cannot overcome the fundamental limits of niobium, given by critical temperature and critical field.

Present research is ongoing in order to identify suitable new materials for coating. Here Nb_3Sn is one promising candidate. With superheating field $B_{\text{sh}} \approx 400\text{ mT}$ accelerating gradients up to 100 MV/m are expected theoretically. The critical temperature $T_c = 18.2\text{ K}$ is higher than the one of niobium ($T_c = 9.25\text{ K}$), which allows operation at higher temperatures [12, 23].

The maximum efficiency of a cooling heat pump, working between two constant temperatures, is given by the Carnot efficiency

$$\eta_c = \frac{T_{\text{cold}}}{T_{\text{warm}} - T_{\text{cold}}}. \quad (2.29)$$

Increasing the operating temperature of a cavity from 2 K to 4 K or 10 K , reduces the electrical power required for cooling by a factor 2 or 5. Regarding the cost of a cryo plant of about EUR 40 million, a relevant amount of money is saved if size and complexity of such a plant is reduced. Furthermore an increased T_c promises lower surface resistance at the same temperature, since $\Delta \propto T_c$ (see eq. 2.23).

One potential issue of superconductors with higher T_c is given by a typically higher Ginzburg-Landau parameter (e.g. $\kappa = \lambda_L/\xi_0 = 20$ for Nb_3Sn). Assuming constant ξ_0 , an increasing penetration depth causes the surface resistance to grow quickly as given by the two-fluid model (see eq. 2.21).

2.3 Superconducting Thin Films

A lower coherence length may cause technological problems. ξ_0 denotes the size of a Cooper pair and therefore gives a length scale on which pairs are sensitive to lattice disturbances. If the coherence length becomes smaller than the thickness of a grain boundary, supercurrents get “trapped” within one grain. The missing link between neighboring grains is expected to cause higher surface resistance, which is the case for high-temperature superconductors like cuprates ($\xi_0 \approx 0.85$ nm). Compared to niobium ($\xi_0 \approx 39$ nm), the coherence length of Nb_3Sn is already smaller by one order magnitude ($\xi_0 \approx 4.5$ nm) [12, 19].

The idea of using multilayer structures denotes another concept to achieve accelerating gradients beyond the limit of niobium: By coating subsequent layers of insulating (I) and superconducting (S) films in the order of λ_L , the penetration of vortices can be suppressed. By using a single S-I-S structure on bulk niobium, the critical magnetic field is already expected to be high enough, allowing an accelerating gradient of 100 MV/m. Provided the availability of appropriate coating technologies, an upgrade towards higher gradients of existing cavities made out of bulk niobium becomes possible [24, 25].

3 The Quadrupole Resonator

The performance of SRF accelerating cavities strongly depends on the surface resistance of the cavity walls. Optimization of surface treatment procedures and research on new materials requires measurements in the $n\Omega$ -range of the RF surface resistance. For this purpose the QPR was developed as a dedicated testing equipment. It allows one to characterize planar circular samples of 75 mm diameter using a calorimetric measurement, which intrinsically has much higher resolution than RF-based surface resistance measurements. The design originates from E. Brigrant and E. Haebel at CERN, where the first QPR was built [26–32]. A second resonator with improved RF parameters, based on that design, was developed at HZB and brought into operation in 2014 [33]. In the following, design and measurement principle of the QPR is presented, with focus on the resonator at HZB.

3.1 RF Design

A schematic view of the QPR is given in figure 3.1. The main components are the sample (yellow) and four quadrupole rods (green): The rods are connected pairwise by a crescent-shaped loop at the bottom and all rods are shortened at the top level. The length of the rods is adjusted to $\lambda/2$ of the baseline operation frequency of 433 MHz. Since higher harmonics of 433 MHz can be excited as well, further operation frequencies are given by 866 MHz and 1.3 GHz. This frequency range covers most of the frequencies used for SRF accelerating cavities. Furthermore, measuring at 433 MHz provides high sensitivity to residual surface resistance due to the comparatively low level of BCS contribution.

Placing the loops at a small distance (0.5 mm) above the sample surface, provides focusing of the RF magnetic field to that area (see. fig. 3.2). By using two pairs of rods the fundamental mode of the setup is quadrupole-like. The screening cavity (red) hosts sample and rods and provides electrical connection of all rods.

The question of implementing an exchangeable (sample) surface inside of an RF-tight volume is solved by using a coaxial structure. The sample is mounted on top of a cylinder which acts as inner conductor of a coaxial line. Due to the exponential decay of quadrupole modes inside coaxial lines, all significant RF losses on the cylinder surface take place on the sample itself. Using two pairs of rods instead of one and hence exciting a quadrupole mode instead of a dipole one provides the advantage of a doubled cut-off frequency (see sec. 4.2).

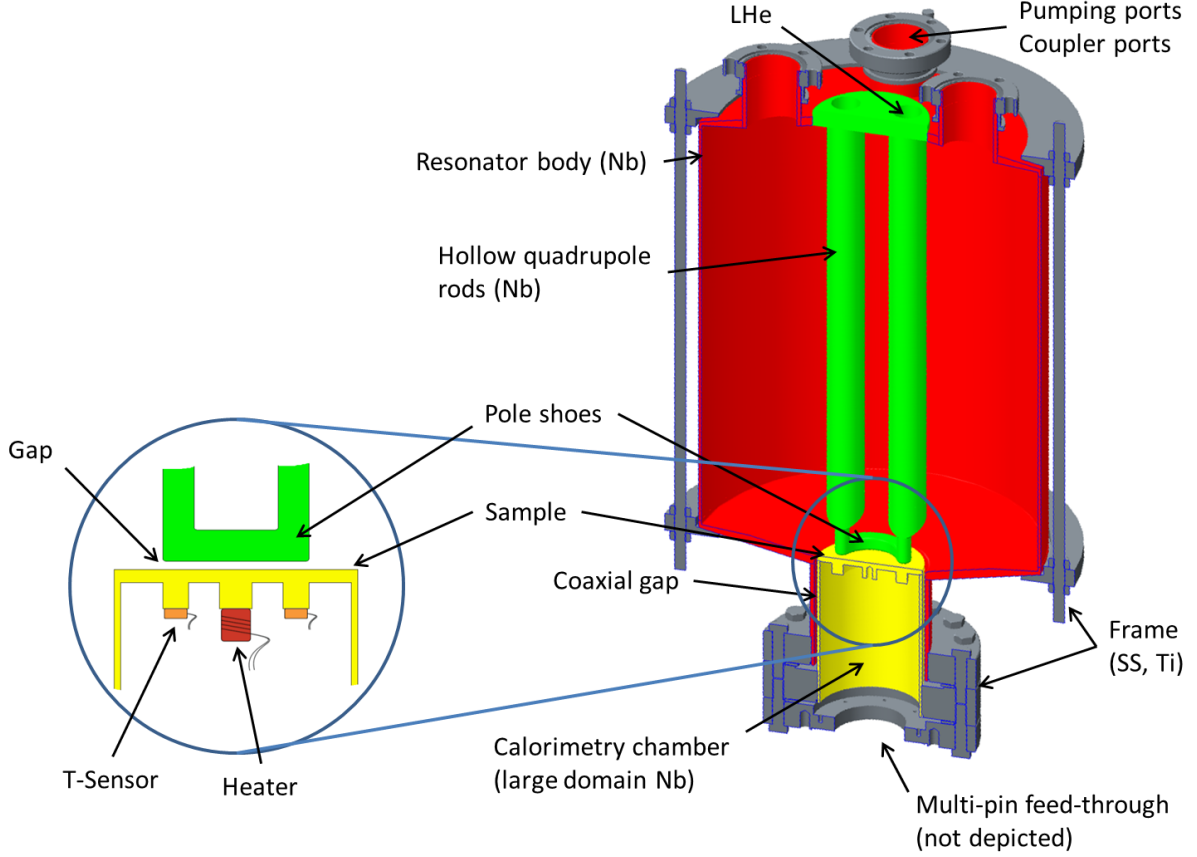


Figure 3.1: Schematic view of the Quadrupole Resonator: Cross-section in the plane of mirror. Property: RF design by Raphael Kleindienst (HZB) [33], mechanical design by Niowave Inc.

For operation the resonator is cooled down to liquid helium temperature using a helium bath cryostat. The quadrupole rods are hollow, allowing liquid helium to cool these regions of high magnetic field. This is important to enable measurements at high field level without quenching the resonator.

The QPR is equipped with two loop-antennas at fixed coupling. The input power coupler is a strongly overcoupled antenna with coupling factor β around 100. The pickup antenna is very weakly coupled ($\beta \approx 10^{-4}$). Microphonics is a known issue of the resonator potentially limiting the RF performance [34]. Due to the strong overcoupling of the input antenna, the bandwidth of the resonator is broadened, helping the phase-locked loop (PLL) to track the resonant frequency. For details on cavity operation the reader is referred to [35].

The strong point of the Quadrupole Resonator is its large and quickly accessible parameter space of magnetic field strength, temperature and frequency. For temperature control the sample is equipped with a resistive DC heater in the center of its bottom. Heat produced there is conducted via the niobium tube to the bottom flange which is in contact with the liquid helium

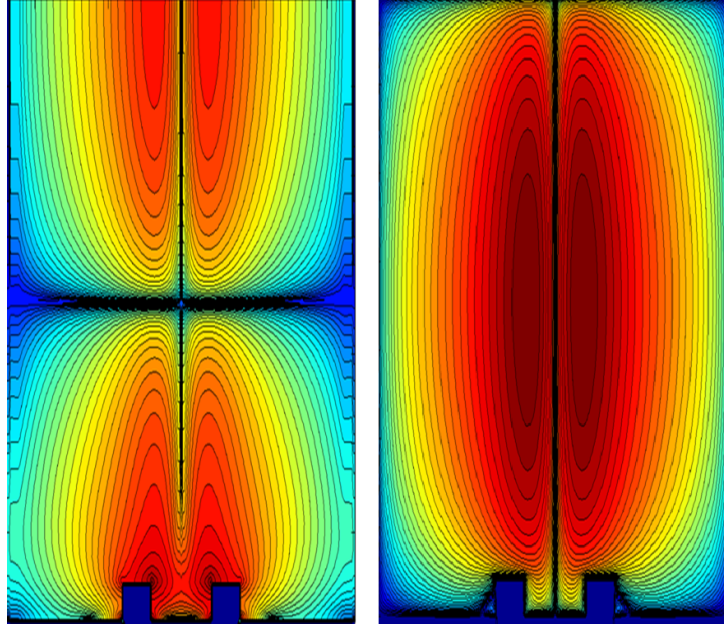


Figure 3.2: *RF Magnetic (left) and electric (right) field distribution inside the QPR for the quadrupole mode at 433 MHz [33].*

(LHe) bath. Due to this long thermal route, the sample is essentially thermally decoupled from the resonator. In this case the LHe bath only defines the minimum operation temperature and keeps the resonator at stable conditions. The sample temperature is defined by the applied heater power. Furthermore, all changes in the RF behavior are caused primarily by the sample, since the resonator is thermally stabilized and the RF magnetic field is focused to the sample surface.

3.2 Surface Resistance Measurement

The QPR measures the RF surface resistance of a sample using an RF-DC compensation technique consisting of two steps. The measurement principle is depicted in fig. 3.3.

1. The sample is heated to the temperature of interest using the DC heater. The heater power P_{DC1} is derived by precisely measuring the voltage drop across the heater and the applied current.
2. In thermal equilibrium the RF input is switched on and the heater power is reduced so, that the temperature of the sample again reaches the initial value. In steady state the reduced heater power P_{DC2} is measured.

Temperatures are measured by calibrated Cernox™ sensors which are placed on the bottom of the sample, right below the region of highest magnetic field. For heater regulation a PID control loop is used.

3.2 Surface Resistance Measurement

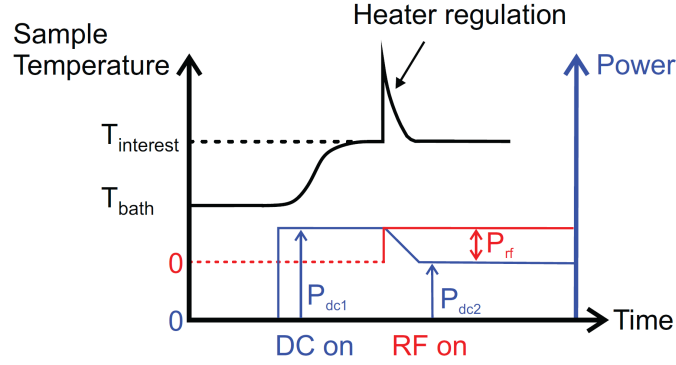


Figure 3.3: Using a calorimetric measurement system the surface resistance of a superconducting sample is derived from a DC measurement [36].

The RF power dissipated on the sample is simply given by the difference in DC heater power. Using eq. 2.4 yields

$$P_{\text{RF}} = P_{\text{DC1}} - P_{\text{DC2}} = \frac{1}{2\mu_0^2} \int_{\text{Sample}} R_s |\vec{B}|^2 dS \approx \frac{1}{2\mu_0^2} R_s \int_{\text{Sample}} |\vec{B}|^2 dS. \quad (3.1)$$

In this setup the surface resistance is assumed to be independent of B and not to vary significantly across the sample surface. Hence R_s may be pulled outside the integral. Solving for the surface resistance leads to

$$R_s = \frac{2\mu_0^2 (P_{\text{DC1}} - P_{\text{DC2}})}{\int_{\text{Sample}} |\vec{B}|^2 dS}. \quad (3.2)$$

The integral in the denominator of this expression is not experimentally accessible. From numerical simulations performed in the optimization process of the QPR for all operation frequencies, the following constants were extracted to relate this integral to a measurable quantity (values for $f = 433 \text{ MHz}$) [33]:

$$\begin{aligned} c_1 &= \frac{B_{\text{Sample, pk}}^2}{\int_{\text{Sample}} |\vec{B}|^2 dS} = 701 \frac{1}{\text{m}^2} \\ c_2 &= \frac{B_{\text{Sample, pk}}^2}{U} = 0.124 \frac{\text{T}^2}{\text{J}} \\ c &= \frac{c_1}{c_2} = \frac{U}{\int_{\text{Sample}} |\vec{B}|^2 dS} = 5654 \frac{\text{J}}{(\text{Tm})^2} \end{aligned} \quad (3.3)$$

Putting 3.3 into 3.2 yields

$$R_s = \frac{2c\mu_0^2 (P_{\text{DC1}} - P_{\text{DC2}})}{U}. \quad (3.4)$$

The stored energy inside the QPR is measured using the pickup antenna. The quality factor of the pickup antenna is defined in the same sense as for an accelerating cavity (see eq. 2.2)

$$Q_t = \frac{\omega U}{P_t}. \quad (3.5)$$

With known Q_t and by measuring the transmitted power P_t , eq. 3.2 becomes an expression of only constants and measurands:

$$R_S = \frac{2c\omega\mu_0^2(P_{DC1} - P_{DC2})}{Q_t P_t} \quad (3.6)$$

P_t is also used to determine the peak magnetic field strength on the sample surface

$$B_{\text{Sample, pk}} = \sqrt{c_2 U} = 352.14 \frac{\text{mT}}{\sqrt{\text{J}}} \sqrt{\frac{Q_t P_t}{\omega}}. \quad (3.7)$$

Besides Q_t , quality factors are defined for the input coupler (Q_e) and the bare resonator (Q_0). In case of a strongly overcoupled input antenna and weakly coupled field probe ($Q_e \ll Q_0 \ll Q_t$), the loaded quality factor (Q_L) of the overall system is dominated by the input coupler

$$\frac{1}{Q_L} = \frac{1}{Q_e} + \frac{1}{Q_0} + \frac{1}{Q_t} \approx \frac{1}{Q_e}. \quad (3.8)$$

During commissioning of the QPR, Q_t has to be measured. This is done via an emitted power measurement: If the incident power is switched off after the cavity arrived in a steady state, the stored energy decays exponentially. Due to the strong overcoupling, approximately all energy is emitted through the input coupler, while losses on the cavity walls as well as through the pickup port are negligible. The emitted power is integrated using a fast power meter

$$U \approx \int_{t_0}^{\infty} P_e dt = \int_{t_0}^{\infty} P_r dt \approx \sum_m^N (P_r) \Delta t \quad (3.9)$$

with the sample point m where the incident power is switched off and the total number of sample points N . In addition the transmitted power for the steady state just before switching off the RF power is measured. Now the quality factor of the field probe can be calculated using eq. 3.5.

With this calorimetric measurement the RF surface resistance can be measured at sub-n Ω resolution. Using an RF power measurement instead, considers the total RF dissipation of the QPR system. Especially when characterizing samples with low loss, R_S would be overestimated systematically due to losses in other regions of the QPR.

The calorimetric measurement relies on the reduction of DC heater power in case of RF heating. Thus the RF dissipation without DC heating defines the minimum measurement temperature at a given field level. The maximum temperature is restricted by thermal runaway of the sample. If the RF duty cycle is reduced by using pulsed power, measurements at lower temperature and close to T_c become possible.

3.3 Measuring Penetration Depth and Further Properties

As seen in sec. 2.2, the RF penetration depth rapidly changes with temperature (see eq. 2.12):

$$\lambda(T) = \frac{\lambda_0}{\sqrt{1 - \left(\frac{T}{T_c}\right)^4}} \quad (3.10)$$

The Slater perturbation theorem describes the shift of resonant frequency in case of a changing volume of a resonant cavity [37,38]:

$$\frac{\Delta f}{f} = \frac{\frac{1}{4} \int_V^{V+\Delta V} \left(\epsilon_0 |\vec{E}|^2 - \mu_0 |\vec{H}|^2 \right) dV}{U}. \quad (3.11)$$

Applied to the QPR, a negative shift of resonant frequency is caused by an increasing penetration depth, which effectively enlarges the cavity volume in a region of high magnetic field. Heating the sample close to T_c yields a measurable frequency shift which is only related to the increase of penetration depth on the sample, since resonator and calorimetry chamber are decoupled thermally [34]. By analogy to the geometry factor of an accelerating cavity (see eq. 2.5) the geometry factor of the sample is defined

$$G_{\text{Sample}} = R_S Q_{\text{Sample}} = R_S \frac{\omega U}{P_{\text{Sample}}} \quad (3.12)$$

which only considers RF dissipation on the sample surface. G_{Sample} is known from simulations, hence an observed shift of frequency can be translated into a change of penetration depth [34]:

$$\Delta \lambda = \lambda(T) - \lambda_0 = -\frac{G_{\text{Sample}}}{\pi \mu_0 f^2} \Delta f \quad (3.13)$$

Performing a least squares fit to the measured data yields the penetration depth at $T = 0\text{ K}$ (λ_0). T_c can be both, input from literature or derived from the fit as well. From λ_0 the electron mean free path ℓ and the Residual Resistance Ratio (RRR) are obtained [12,39]:

$$\lambda_0(\ell) = \lambda_L \sqrt{1 + \frac{\pi \xi_0}{2\ell}} \iff \ell = \frac{1}{2} \cdot \frac{\pi \xi_0}{\left(\frac{\lambda_0(\ell)}{\lambda_L}\right)^2 - 1} \quad (3.14)$$

$$\text{RRR} = \frac{\ell [\text{nm}]}{2.7} \quad (3.15)$$

The values of London penetration depth λ_L and BCS coherence length ξ_0 are taken from literature and assumed to be independent of temperature [34,40].

Using the QPR a second method is available to obtain the RRR of a sample. Following the basic definition of RRR (see eq. 2.27) a direct measurement is possible, if the sample is in the normal conducting state at low temperature. In case of a normal conductor with skin depth δ the RF surface resistance is related to RRR as follows

$$R_S = \frac{1}{\sigma\delta} = \frac{\sqrt{\pi f \sigma \mu}}{\sigma} = \sqrt{\frac{\pi f \mu_0}{\sigma_0 \cdot \text{RRR}}} \quad (3.16)$$

with $\mu = \mu_0$ and the conductivity of niobium at room temperature $\sigma_0 = 6.58 \cdot 10^6 (\Omega\text{m})^{-1}$ taken from literature [41]. Due to the thermal decoupling of calorimetry chamber and resonator, the sample can be heated to 13 K without warming the resonator significantly. Now the resonator becomes undercoupled and the quality factor of the sample dominates, since the resonator chamber remains superconducting:

$$\frac{1}{Q_L} = \frac{1}{Q_e} + \left(\frac{1}{Q_{\text{Resonator}}} + \frac{1}{Q_{\text{Sample}}} \right) \approx \frac{1}{Q_e} + \frac{1}{Q_{\text{Sample}}} \quad (3.17)$$

The loaded quality factor is measured using a vector network analyzer. Taking the external quality factor from previous measurements, the RRR is derived using G_{Sample} (eq. 3.12)

$$\text{RRR} = \frac{\pi f \mu_0}{\sigma_0 R_S^2} = \frac{\pi f \mu_0}{\sigma_0} \left(\frac{Q_{\text{Sample}}}{G_{\text{Sample}}} \right)^2. \quad (3.18)$$

Eq. 3.16 only applies for the normal skin effect. For high RRR and/or high frequency the anomalous skin effect has to be taken into account. In this case the mean free path becomes larger than the skin depth and the assumption of a constant electric field within ℓ breaks down. Hence, the local Ohm's law has to be replaced by an integral, considering electrons "escaping" from the skin depth. The dimensionless parameter α_s is introduced to distinguish between normal and anomalous skin effect

$$\alpha_s = \frac{3}{4} \mu_0 \omega \left(\frac{1}{\rho \ell} \right) \ell^3 \quad (3.19)$$

with resistivity $\rho = 1/\sigma$. The normal skin effect and hence eq. 3.16 applies for $\alpha_s \leq 0.016$ [12]. Using eqs. 2.27 and 3.15, α_s can be rewritten as

$$\alpha_s = \frac{3}{4} \mu_0 \omega \left(\frac{\sigma_0}{2.7 \cdot 10^{-9}} \right) (2.7 \cdot 10^{-9} \text{RRR})^3 \approx 2.84 \cdot 10^{-10} \frac{f}{\text{MHz}} (\text{RRR})^3 \quad (3.20)$$

in case of niobium at cryogenic temperatures. For the lowest operating frequency of the QPR ($f = 433 \text{ MHz}$), this threshold yields $\text{RRR} = 50$. In the anomalous limit ($\alpha_s \rightarrow \infty$), the surface resistance is given by [12]

$$R_{S, \text{anom.}} = \left[\sqrt{3} \pi \left(\frac{\mu_0}{4\pi} \right)^2 \right]^{1/3} \omega^{2/3} (\rho \ell)^{1/3} \approx 9.588 \cdot 10^{-3} f^{2/3} \frac{\text{m}\Omega}{(\text{MHz})^{2/3}}. \quad (3.21)$$

3.3 Measuring Penetration Depth and Further Properties

Since in the anomalous limit the surface resistance is independent of the DC resistivity, this measurement principle cannot be used to determine the RRR of highly pure samples.

Furthermore, the critical magnetic field $H_c(T)$ of the sample can be determined by pulsing the incident RF power at a given temperature of interest. The RF power level is increased continuously until a quench of the sample is triggered instantly. The actual critical field is deduced from the maximum transmitted power detected by the pick-up antenna, using eq. 3.7. This measurement is only possible for temperatures close to T_c , since the incident power has to be low enough to avoid quenching the resonator chamber itself. $H_c(0\text{ K})$ is derived from a fit to the data using [12]

$$H_c(T) = H_c(0\text{ K}) \left[1 - \left(\frac{T}{T_c} \right)^2 \right]. \quad (3.22)$$

4 Simulations

4.1 Introduction

In the design of a demountable calorimetry chamber one has to assume that the outer surface of the chamber cannot remain perfectly smooth. Since the local RF field is very sensitive to surface effects, possible issues have to be considered in the design process. Looking at the outer surface of the chamber, a separability results in two touching cylinders with “something” in between. That “something” at the contact area of the cylinders can contain any imperfection, potentially causing problems while measuring with the Quadrupole Resonator (QPR). Therefore, numerical simulations are used to estimate possible influences which then are fed back into the design process. An exploded view of the demountable calorimetry chamber in the final design is given in figure 4.1. Technical drawings are provided and discussed in chapters 5 and 6.

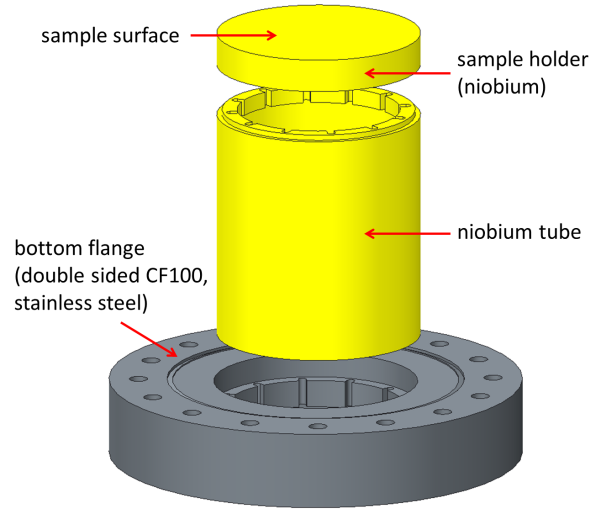


Figure 4.1: *Exploded view of the demountable calorimetry chamber.*

One important question to be answered by these simulations is what the minimum height of the sample carrier must be. For coating, the minimal height is desired but then the contact area of the chamber parts is moved into a region of higher RF field. Crucial design criterion is to ensure a safe operation of the QPR up to high fields, meaning that any additional power dissipation with impact on the temperature distribution of the sample has to be avoided. Possible structures which are investigated here are deviating radii and pits or bumps appearing due to uneven contacting surfaces. In this chapter only the contact area of sample holder and tube is

4.2 Theory and Analytical Considerations

investigated. By construction the RF fields at the bottom flange are negligible, hence a contact area there will not cause any disturbing RF effects.

In the following section some theoretical background concerning the RF field in a coaxial structure is presented in order to get an analytical estimate on the impact of imperfections. This is possible for deviations of the radius of the chamber and – to some extent – for the scenario of a circumferential gap between sample holder and tube. For the investigation of the quantitative impact of pits and bumps on the field, further numerical simulations were performed in two steps. First, the worst-case scenario of a circumferential gap was investigated and compared to theory. Afterwards, less pessimistic assumptions were made which led to considering spatially limited gaps. Nevertheless analytical expressions and physical arguments are available to cross-check and discuss the results of the simulations.

4.2 Theory and Analytical Considerations

4.2.1 Radial Deviations

The calorimetry chamber of the QPR is decoupled from the resonator via a coaxial structure. Therein the chamber represents the inner conductor (see sec. 3.1). The measurement principle requires that all significant RF losses on this inner conductor take place on the sample surface. Otherwise, the sample is heated up by additional RF dissipation on the chamber wall, and the surface resistance of the sample surface is overestimated. Since the whole chamber is made out of (superconducting) niobium significant losses can only be suppressed by damping the field.

For a general constant-cross section wave guide in z -direction a traveling wave can be written in the form

$$\Theta_z = \vartheta_z(x, y) e^{i(\omega t - k_z z)} \quad (4.1)$$

with $\vartheta_z(x, y)$ containing all amplitude information. The exponential function describes the spatial oscillation in z -direction and over time. The angular frequency ω is connected to the propagation constant k_z as follows:

$$\frac{\omega^2}{c^2} = k^2 = k_c^2 + k_z^2 \quad (4.2)$$

$$\Leftrightarrow k_z = \pm \sqrt{\frac{\omega^2}{c^2} - k_c^2} \quad (4.3)$$

with the cut-off wave number k_c determined by the geometry of the waveguide. Frequencies below cut-off

$$f_c = \frac{\omega_c}{2\pi} = \frac{ck_c}{2\pi} \quad (4.4)$$

cause k_z to be imaginary and the propagation is damped exponentially [42]. In general cut-off wave numbers cannot be determined analytically, but in case of a coaxial line approximation formulas are available as functions of outer and inner diameter (D_o resp. D_i) [43]:

$$\text{TE}_{m1} : k_c \approx \frac{4m}{D_o + D_i} \quad m = 1, 2, \dots \quad (4.5)$$

$$\text{TE}_{mn} : k_c \approx \frac{2\pi(n-1)}{D_o - D_i} \quad n = 2, 3, \dots \quad (4.6)$$

$$\text{TM}_{mn} : k_c \approx \frac{2\pi n}{D_o - D_i} \quad n = 1, 2, \dots \quad (4.7)$$

The TE-11 mode has the lowest cut-off frequency, in this case $D_o = 77$ mm and $D_i = 75$ mm yield $f_c \approx 1.3$ GHz. Quadrupole modes which are the operating modes of the resonator are TE-21 like [34] with cut-off frequency twice as big ($f_c \approx 2.5$ GHz) and so all three operating modes are damped as desired. TM modes and higher TE modes do not have to be considered any further since their cut-offs scale with $f_c \propto (D_o - D_i)^{-1}$ which is far beyond any operation frequency. Radial deviations of the calorimetry chamber are – estimated conservatively – smaller than 2 mm reducing the lowest cut-off not more than 15 MHz. Hence his effect can be neglected and radial deviations are not considered any further.

4.2.2 Magnetic Field Enhancement

The RF wave used for operation of the QPR is damped exponentially in the coaxial structure (see sec. 4.2.1). Since the demountable sample carrier should be as short as possible one has to assume a significant residual field on the contacting surface. For RF measurements it is crucial that all RF losses on the surface of the calorimetry chamber take place on the sample surface. Hence a trivial condition is to ensure the superconducting state of niobium of the chamber. Moreover any field level comparable to greater than that on the sample surface may at most be tolerated on very small areas.

In this section, the effects of irregularities like pits, bumps or gaps occurring at the contacting surface of both parts of the chamber are discussed. Near these structures an enhancement of the magnetic field is expected. The Magnetic Field Enhancement (MFE) factor β is introduced and defined as follows:

$$\beta = \frac{H}{H_0} \quad (4.8)$$

with the locally enhanced magnetic field H with respect to H_0 , representing the magnetic field without any local imperfection. For two-dimensional pits of several shapes, the MFE factor can be determined analytically using the method of conformal mapping [44, 45].

A realistic worst-case scenario is investigated by the case of a well-like pit. This is a two-dimensional structure of rectangular cross-section and can be applied to a circumferential gap

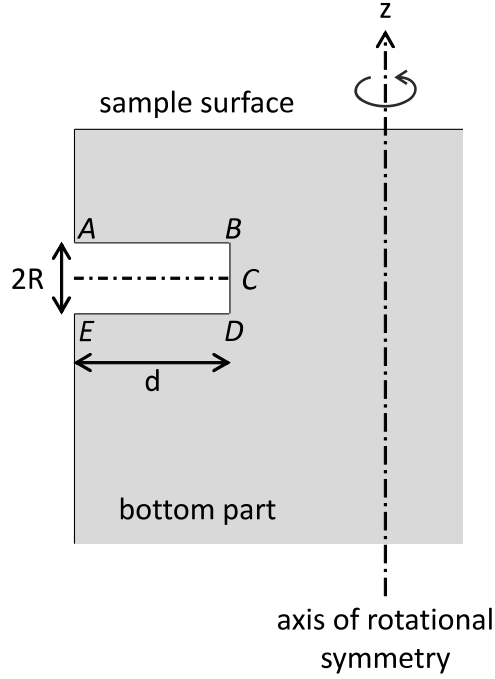


Figure 4.2: Well-like pit at the contact between top and bottom part of the chamber. Grey colored regions correspond to a superconductor in the Meissner state.

between top and bottom part of the chamber (see fig. 4.2). In the calculation it is assumed that the surrounding material (gray colored) is a superconductor in the Meissner state. Furthermore the depth of the well d is large compared to half of the width ($d \gg R$).

In the vicinity of the corners A and E the MFE factor is given by [45]

$$\beta(r) = \left(\frac{2}{3\pi} \frac{R}{x} \right)^{\frac{1}{3}} \quad (4.9)$$

where x denotes the distance from one of these corners. At the points A, B, C, D and E the MFE factor is given by

$$\begin{aligned} \beta(A) &= \beta(E) = \infty \\ \beta(B) &= \beta(D) = 0 \\ \beta(C) &\approx e^{-\frac{\pi}{2} \frac{d}{R}} \end{aligned} \quad (4.10)$$

The solution of $\beta = \infty$ is unphysical. The MFE becomes finite, if the sharp edges at points A and E are replaced by a curvature with radius r . In this case eq. 4.9 yields

$$\beta_{\max} \approx \beta(r) = \left(\frac{2}{3\pi} \frac{R}{r} \right)^{\frac{1}{3}}. \quad (4.11)$$

This result is confirmed by numerical simulations using SLANS2 [46]. Well-like pits with varying values for r/R have been studied in the geometry of a pill-box cavity at 2 GHz. These pits are

presented as a hole on the axis of the cavity (=beam pipe). The cavity is excited in the mode TE_{111} which has the maximum magnetic field located at the center of the end plates. The simulations confirm the scaling of the MFE factor to be $\beta \propto \left(\frac{R}{r}\right)^{\frac{1}{3}}$ for ratios $r/R \lesssim 0.2$. For the simulations performed here, this condition is always fulfilled.

Following the analytical calculation in the limit of deep holes ($d \gg R$) the MFE factor is independent of the depth of the hole. This is also an outcome of the simulations and the condition of “deep holes” is achieved for $d \geq 1.5R$ [46].

One question remains: What assumption can be made to estimate the minimal radius of (relevant) structures? Otherwise no upper limit can be set to the MFE factor and every imperfection could cause a quench of the calorimetry chamber.

To answer this question a physical argument is available [47]: Even if the edge of a structure is (infinitely) sharp, the RF field “sees” an effective radius of curvature R_{eff} due to the penetration depth of an RF wave into a (super-)conducting solid. A simplified model of an infinitely sharp edge and the resulting effective curvature is depicted in figure 4.3. R_{eff} can be then calculated as

$$R_{\text{eff}} = \frac{\delta}{\sqrt{2} - 1} \approx 2.4\delta. \quad (4.12)$$

For a normal conducting object this penetration depth is defined by the skin depth δ , in a superconductor the corresponding length is given by the London penetration depth λ_L . Since λ_L is much smaller than δ the resulting field enhancement is larger. When $\beta H > H_{\text{crit}}$ the edge quenches, R_{eff} suddenly increases and β decreases. If one assumes that the edge is in a state where the outermost part is normal conducting, the MFE factor is calculated for normal conducting niobium with the skin depth δ . In [47] δ is calculated for a frequency of 1.3 GHz and 4.2 K. Scaling down to the operating frequency of the QPR of 433 MHz with $\delta \propto 1/\sqrt{f}$ leads to $\delta = 0.5 \mu\text{m}$ and $R_{\text{eff}} = 1.2 \mu\text{m}$. For following calculations $R_{\text{eff}} = 1 \mu\text{m}$ is used.

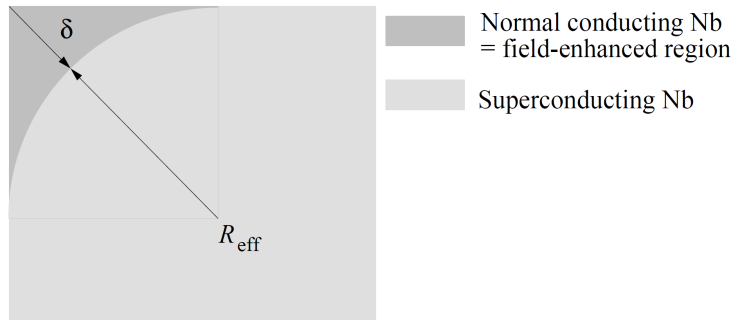


Figure 4.3: Geometry used to estimate the effective radius of curvature “seen” by the RF field at an infinitely sharp edge [47].

The scenarios presented here cannot be applied to the quadrupole resonator completely. The 2-D theory implies rotational symmetry in 3-D, which is not given for the RF fields in the QPR. Therefore numerical simulations are performed which are presented in the following. Nevertheless,

4.4 Geometry

approximation formulas obtained from theory can be used as an estimate and for cross-checking. First the worst-case scenario of a “well-like pit with sharp edges” is investigated. The MFE factor diverging at the edge can then be discussed using the physical argument of effective rounding. In a second step the circumferential gap is replaced by spatially limited gaps.

4.3 Software

In the following the computer program COMSOL Multiphysics (v. 4.4.0) is used for RF simulations [48]. This program uses the finite element method to solve physical problems described by differential equations. Problems can be solved from 0-D up to 3-D geometries which do not have to show any symmetry. The mesh for computation can be defined piecewise which allows one to locally to increase the mesh density. This provides an opportunity to resolve small-sized structures despite a comparatively large volume of the overall geometry.

The RF eigenmodes of the QPR could be determined using only a quarter of its volume by applying appropriate boundary conditions. In this work it was decided to use a fully three dimensional model to obtain maximal flexibility in choosing the geometry of imperfections to be simulated.

4.4 Geometry

During measurements the QPR is operated at one of its quadrupole modes of 433, 866 or 1300 MHz. Thus the impact of imperfections of the calorimetry chamber on the RF has to be evaluated at these eigenmodes of the resonator. Therefore the whole resonator is modeled with COMSOL and the eigenmode solver is used. Using the finite element method the general equation

$$\nabla \times \frac{\nabla \times \vec{E}}{\mu_r} - k_0^2 \left(\epsilon_r - \frac{j\sigma}{\omega\epsilon_0} \right) \vec{E} = 0 \quad (4.13)$$

with eigenvalue

$$\lambda = -j\omega + \delta \quad (4.14)$$

is solved for the field \vec{E} [49]. The volume of the resonator is “filled” with vacuum which has no conductivity and so the term proportional to σ drops out. The boundaries of the geometry represent the surface of the resonator, made out of superconducting niobium. Hence the corresponding boundary condition is that of a perfect conductor:

$$\vec{n} \times \vec{E} = 0 \quad (4.15)$$

In this lossless case the eigenvalue λ is only imaginary representing the resonance frequency ω .

The solution is then normalized manually to a maximal magnetic field of 150 mT on the sample surface. For this a color plot with smoothed data is used. During first tests the QPR quenched at a magnetic field level of about 125 mT on the sample. Using the mentioned normalization the field strengths presented here can be regarded as upper limits.

Since the simulation only has to provide the correct frequency and RF field distribution at the entrance of the coaxial structure the geometry of the resonator itself can be simplified. This step reduces the number of mesh points and so the computational effort. The QPR is modeled as follows, important assumptions or approximations are mentioned:

- The resonator is built as a cylinder with radius $r_{\text{qpr}} = 105 \text{ mm}$ and height $h_{\text{qpr}} = 323 \text{ mm}$. There are no ports or the like at the top side and also the bottom of the resonator is flat.
- The quadrupole rods are modeled with 4 cylinders which are connected to the top plate of the resonator. $r_{\text{rod}} = 13 \text{ mm}$, $h_{\text{rod}} = 292 \text{ mm}$
- The loops are extruded from a segmented annulus (see fig. 4.4) with a distance to the sample surface of 1 mm. They are supported by 4 small cylinders ($r = 5 \text{ mm}$) which are connected to the rods by truncated cones with decentered tips.
- As a sample a disk with diameter of 74 mm is used.
- The coaxial gap between resonator and calorimetry chamber is modeled using an annulus extruded to a height of 80 mm. The radial width of the gap is 1.5 mm.

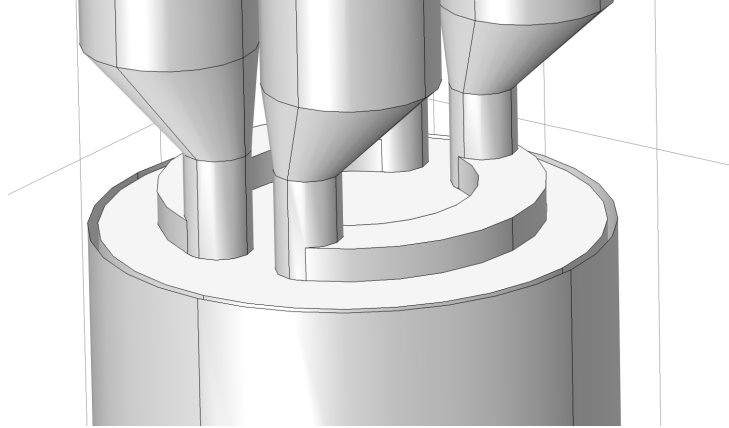


Figure 4.4: *Geometry of quadrupole rods and loops used for simulations.*

Neither the transitions of components nor sharp edges are rounded. This has only little effect on volume effects like the resonance frequency or the selection of the global RF mode which are of primary concern. Surface fields near sharp edges – especially on the rods and the loops – will be enhanced arbitrarily due to infinite field enhancement. This has to be taken into account when fields in the resonator are discussed. Note that for simulating RF eigenmodes of the resonator, only the vacuum inside has to be modeled. All metallic surfaces are treated as perfect conductors

4.5 Step 1: Circumferential Gap

having infinite conductivity. Doing so saves computing resources since all surfaces are infinitely thin and no metallic volume has to be modeled. The impact of the RF surface resistance on the fields is a higher-order effect and is neglected in this work.

4.5 Step 1: Circumferential Gap

The theoretical considerations show that a worst-case scenario for magnetic field enhancement is given by a circumferential gap between upper and lower part of the calorimetry chamber (see sec. 4.2.2). In a first step this structure is investigated numerically. For this purpose the simulation geometry is enlarged as shown in fig. 4.5. The following parameters are available:

- pos_{gap} : Distance between sample surface and upper edge of the gap
- h_{gap} : Height of the gap
- d_{gap} : Depth of the gap

In this parameter space four simulations with different parameter sets have been computed (see tab. 4.1). The baseline geometry is given by the file “qpr_3_mesh_4”.

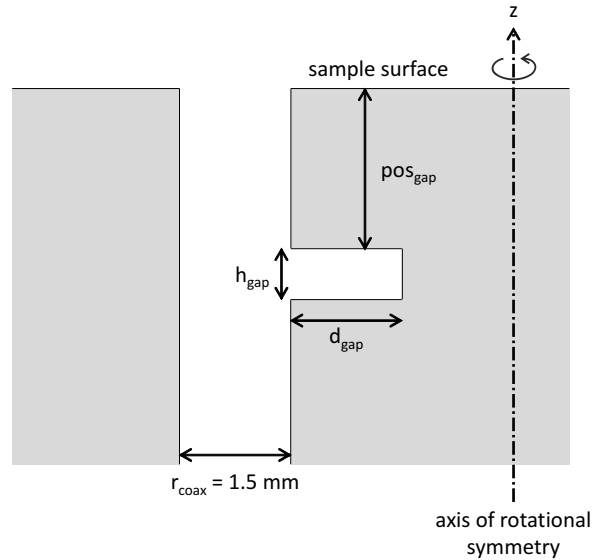


Figure 4.5: Sketch of the inserted circumferential gap.

Name	pos_{gap}	h_{gap}	d_{gap}	resonance frequency
Baseline	5 mm	0.5 mm	1 mm	426.5293 MHz
gap 2.5	5 mm	0.25 mm	1 mm	426.5284 MHz
gap 2.5, slit 4	5 mm	0.25 mm	4 mm	426.5282 MHz
pos 20	20 mm	0.5 mm	1 mm	426.5301 MHz

Table 4.1: Summary of simulations performed in step 1.

The simulations of Shemelin and Padamsee show that the assumption of a deep hole ($d \gg R$) is valid for $d/R \geq 1.5$ (see sec. 4.2.2). With $h_{\text{gap}} = 2R$ this condition is fulfilled in any of the four cases. The resonant frequencies differ only by few kHz. This is expected since an additional volume of about 0.1 cm^3 in a low-field region should not have significant impact on the overall QPR ($V_{\text{QPR}} \approx 10^4 \text{ cm}^3$).

4.5.1 Results of the Baseline Geometry

First of all the results of the baseline simulation geometry are discussed. The other three geometries contain only small changes compared to the baseline and their results are discussed subsequently.

Fig. 4.6 shows the magnetic field strength on the (outer) surface of the calorimetry chamber as a color plot with the surface currents depicted by red arrows. Note that length and color scales are different on the sample surface and on the outer wall of the chamber. On the sample the field is focused by the pole shoes of the quadrupole rods (loops) and the current flows circularly. On the walls of the calorimetry chamber the magnetic field strength decreases with increasing distance into the coaxial structure as qualitatively expected. The maximum field in the coaxial structure is, in contrast to the field on the sample, localized at the opening between the loops. Therefore this location is of interest for further investigations and will be referred to as 90° later.

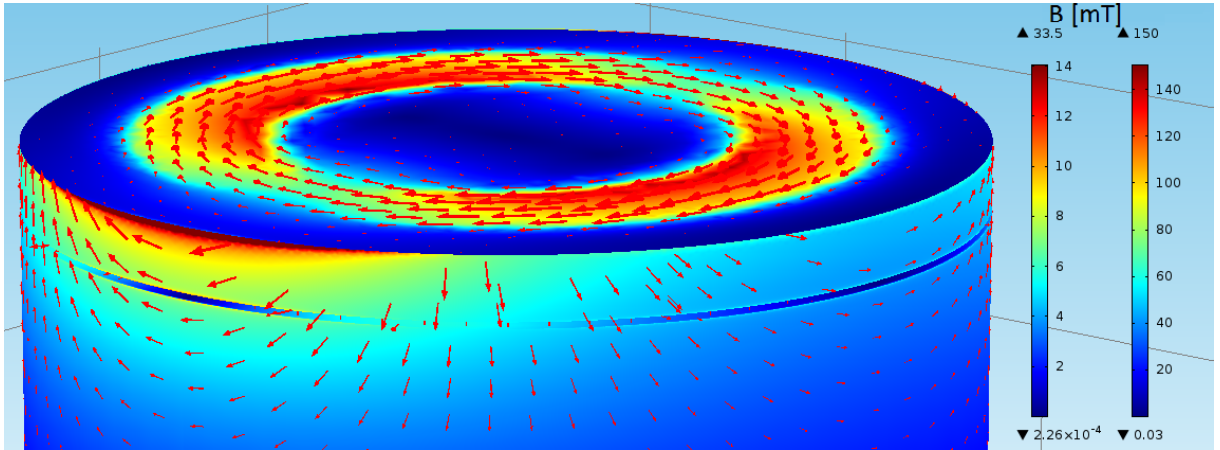


Figure 4.6: Color plot: Magnetic field on the surface of the calorimetry chamber. Surface currents are shown as red arrows. Note: Length and color scales are different for sample (right color scale) and chamber surface (left scale).

The absolute value of the surface current density is directly proportional to the magnetic field and so the maximum current is also located at that spot. The direction of the current here is parallel to the inserted circumferential gap. This case also applies to 0° right at the middle of the loops. A potentially critical location is located at 51° , where the current flows perpendicular

4.5 Step 1: Circumferential Gap

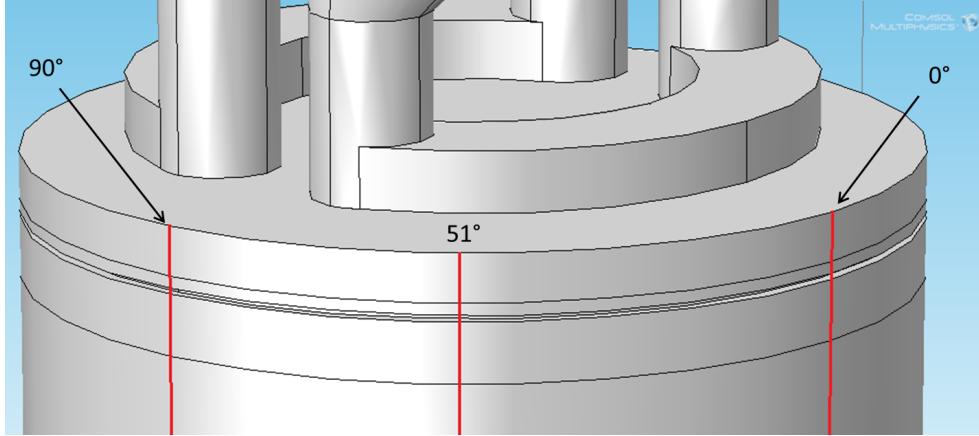


Figure 4.7: Visualization of cut lines in the coaxial structure. Only the inner surface of the coaxial structure is shown.

to the gap. For these locations (0° , 51° and 90°) cut lines are defined in z -direction (vertical) and the fields are investigated quantitatively (see fig. 4.7).

Fig. 4.8 shows the magnetic field for the baseline simulation geometry in the coaxial structure on the cut lines defined in fig. 4.7. The gap at $z = -5$ mm (illustrated by dashed vertical lines) causes field enhancement like qualitatively expected. The region of field enhancement is confined vertically within 1 mm. Note that the cut line at 51° does not show any field enhancement. Due to the perfectly conducting surface the surface current can take the “detour” through the gap without disturbance. Apart from this vertical position and the first 3 mm of the coaxial structure, the magnetic field decays exponentially until $z \approx -45$ mm (linear decrease in semi-logarithmic plot). Approaching the bottom end of the coaxial structure, the curves diverge due to the perfectly conducting boundary condition there. The evanescent wave still carries the characteristics of a TE_{21} mode with roots of the magnetic field at multiples of 90° . In order to obtain a numerical comparison between theory and simulation an exponential function is fitted to the data for all three cut lines with $z \in [-10 \text{ mm}; -40 \text{ mm}]$. The results are as follows:

cut line	$ k_z \text{ [m}^{-1}\text{]}$
0°	37.6
51°	53.6
90°	67.7

The approximation according to eq. 4.5 yields

$$\begin{aligned}
 |k_z| &= \sqrt{k_c^2 - k^2} \approx \sqrt{\left(\frac{4m}{D+d}\right)^2 - \left(\frac{2\pi f}{c}\right)^2} \\
 &\approx \sqrt{\left(\frac{8}{74 \text{ mm} + 77 \text{ mm}}\right)^2 - \left(\frac{2\pi \cdot 433 \text{ MHz}}{c}\right)^2} = 52.2 \text{ m}^{-1}
 \end{aligned}$$

using $m = 2$ because of the TE_{21} -like quadrupole mode. This calculated value lies well between the ones obtained from simulation. The spread among the fitted values can be explained by the deviation of the field from a TE_{21} mode at the entrance of the coax due to the quadrupole loops.

Now the magnetic field propagating into the inserted gap is investigated at the positions 51° and 90° . Therefore two horizontal cut lines on the upper surface of the gap are defined in radial direction. In fig. 4.9 the field is depicted on these cut lines. At the entrance of the gap the field enhancement is equal to values of the cut lines depicted in fig. 4.8 which confirms the consistency of both plots. As expected from the color plot (see fig. 4.6) the magnetic field at 51° does not vary significantly with the radius r since the surface currents take the unperturbed route through the gap at this position.

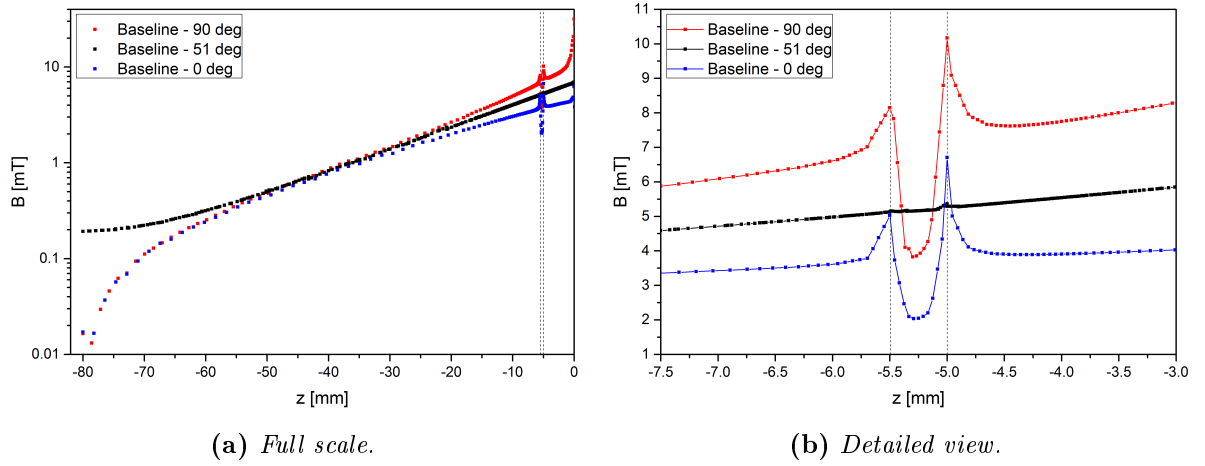


Figure 4.8: Magnetic field on cut lines in the coaxial structure for the baseline simulation geometry. The region of circumferential gap is highlighted by dashed lines.

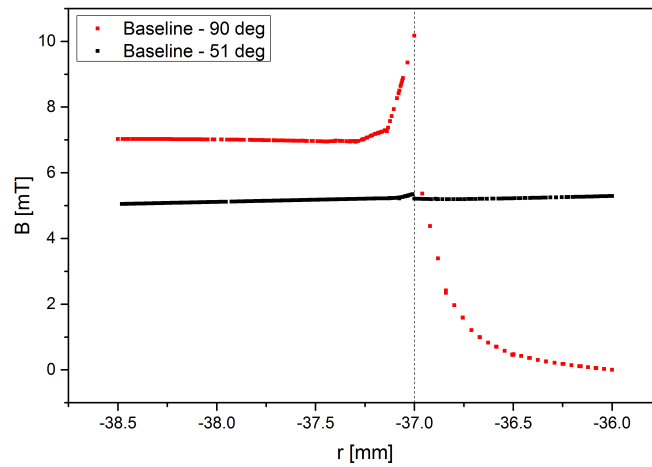


Figure 4.9: Magnetic field on cut lines propagating into the circumferential gap for the baseline simulation geometry. The entrance of the gap is highlighted by a dashed line.

4.5 Step 1: Circumferential Gap

4.5.2 Results from Simulation Geometry Variations

Apart from the baseline simulation geometry three different layouts of a circumferential gap have been simulated (see tab. 4.1). The questions to be answered are:

- How do the relevant quantities scale towards changes in geometry?
- How stable are the results towards changes in mesh density?

All simulations have been normalized equally to a maximal magnetic field on the sample surface of 150 mT and may be compared quantitatively. In fig. 4.10 the fields inside the coaxial structure on the cut line at 90° are depicted for all simulations. It is obvious that the exponential damping of the RF propagating into the coaxial structure is not disturbed except for local field enhancement close to the gap. Neither height or depth nor the position of the gap has an impact on that.

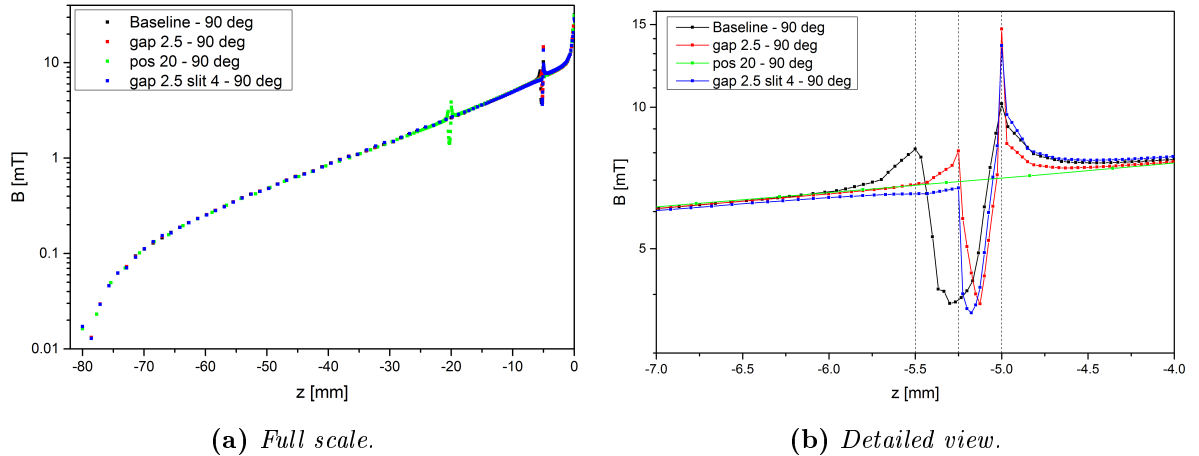


Figure 4.10: Magnetic field on cut lines in the coaxial structure for all simulation geometries at position 90° . The entrance of the gap is highlighted by a dashed line.

In the meshing procedure a surface mesh is created first. Afterwards this two-dimensional mesh is expanded to fill the volume of the geometry. Due to the changes among the simulation geometries the used meshes are not identical. By comparing the results from significantly different meshes, numerical issues from mesh effects can be excluded: Near the inserted circumferential gap the mesh density is enhanced locally to obtain the best resolution possible. This enhancement is clearly visible by looking at the density of data points. For the simulation “pos_20” this densification is also concentrated in the vicinity of the gap only. This leads to a coarser mesh in the upper part of the coaxial structure. Fig. 4.10b depicts that the lower mesh density leads to an equal field distribution which is an argument for well consistent results.

Due to the construction of a surface mesh as first step of the meshing procedure, every edge has to contain mesh points. Hence the field enhancement at the edge of the gap may not be consid-

ered, since the MFE factor diverges here. Using the physical argument of effective rounding (see sec. 4.2.2) with $r_e = 1 \mu\text{m}$ and the analytical calculation of [45] (see eq. 4.9) leads to

$$\beta(h_{\text{gap}}) = \left(\frac{2}{3\pi} \frac{h_{\text{gap}}/2}{1 \mu\text{m}} \right)^{\frac{1}{3}} \approx 0.47 (h_{\text{gap}} [\mu\text{m}])^{\frac{1}{3}}$$

$$\beta(250 \mu\text{m}) = 3.0$$

$$\beta(500 \mu\text{m}) = 3.8.$$

The magnetic fields inside the circumferential gap for all simulations on cut lines at 51° and 90° are depicted in fig 4.11. At position 51° an increase of magnetic field with decreasing radius r is observed, especially for $d_{\text{gap}} = 4 \text{ mm}$. This is a purely geometric effect: In the present case of a constant current the surface current density has to grow with decreasing radius, since the area which conducts this current is decreasing.

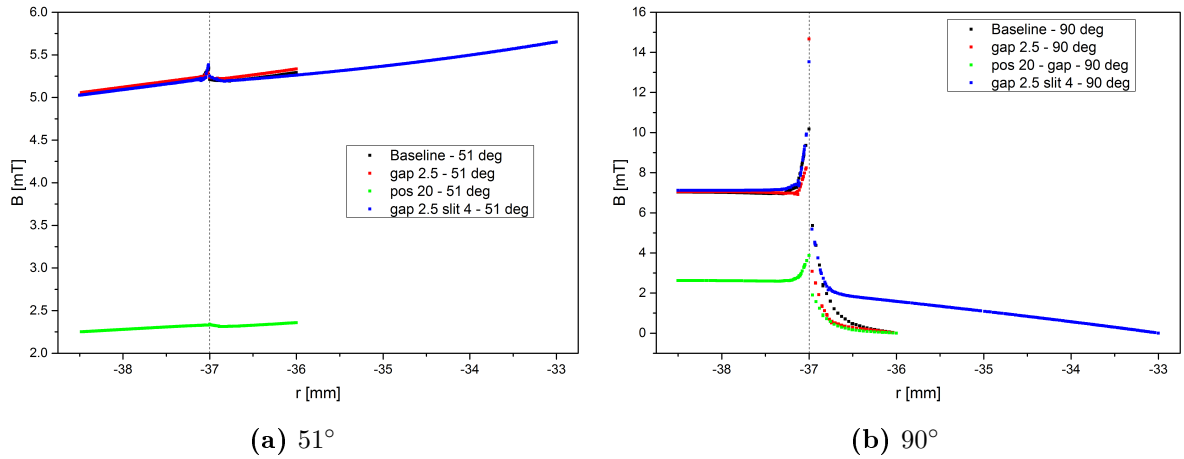


Figure 4.11: Magnetic field on cut lines in the circumferential gap for all simulation geometries at positions 51° and 90° . The entrance of the gap is highlighted by a dashed line.

In conclusion this scenario of a circumferential gap may be tolerated in reality, if a MFE factor up to 4 is accepted and if the inner walls of a circumferential gap provide an intact superconducting surface. The requirement on the inner walls of the gap originates from the surface currents at the 51° position. The “detour” for currents across the gap without disturbance (especially without field enhancement) in this simulation is possible due to the perfectly conducting surface there. In practice the requirement of completeness seems to be challenging since the gap originates from imperfections of the mechanical contact which cannot guarantee an unperturbed electrical contact everywhere.

4.6 Step 2: Separated Gaps

In this section a less pessimistic scenario of imperfections at the contact of upper and lower part of the calorimetry chamber is presented. On the supposition of a mechanical design which is optimized for a good electrical contact of the RF surfaces, a circumferential gap is prevented. The simulation geometry of step 1 is changed such that azimuthally limited pits are considered. Hence the parameter space (see fig. 4.5) is extended by the width w_{gap} and the azimuthal position of these structures.

The simulations performed in step 1 yield RF surface currents flowing perpendicular to the circumferential gap at four positions (51° , 129° , 231° , 309°). At these locations the magnetic field inside the circumferential gap does not decay but stays constant (see fig. 4.9). Now limited gaps are used to estimate the maximal size of structures at that position not disturbing the current distribution on the outer surface of the calorimetry chamber. These gaps will be sufficiently small for the magnetic fields to decay inside, and preventing the surface currents from entering the gaps. In this case the requirement of an intact superconducting surface on the inner walls of the gaps may be relaxed. The simulations from above also show that the parameters pos_{gap} , d_{gap} and h_{gap} do not have any impact on the overall field distribution inside the coaxial structure. Therefore these parameters are not varied here and the following values have been chosen:

parameter	value
pos_{gap}	5 mm
d_{gap}	2.25 mm
h_{gap}	0.5 mm

With $d_{\text{gap}} = 2.25 \text{ mm} = 4.5 h_{\text{gap}}$ the gaps may again be treated as “deep”.

Fig. 4.12 shows the normalized magnetic field inside these limited gaps of different width on a cut line in radial direction. The maximum value for the magnetic field varies between 4.9 mT and 5.2 mT (with sample peak field normalized to 150 mT) which is consistent with step 1 (see fig. 4.9 and fig. 4.11b). The cut line for plotting is placed radially on the middle of the upper surface of these gaps.

As depicted in fig. 4.13 the decay of magnetic field inside the limited gaps strongly depends on the gap width. A damping of field level larger than 90 % can only be achieved for a gap width smaller than 2.5 mm.

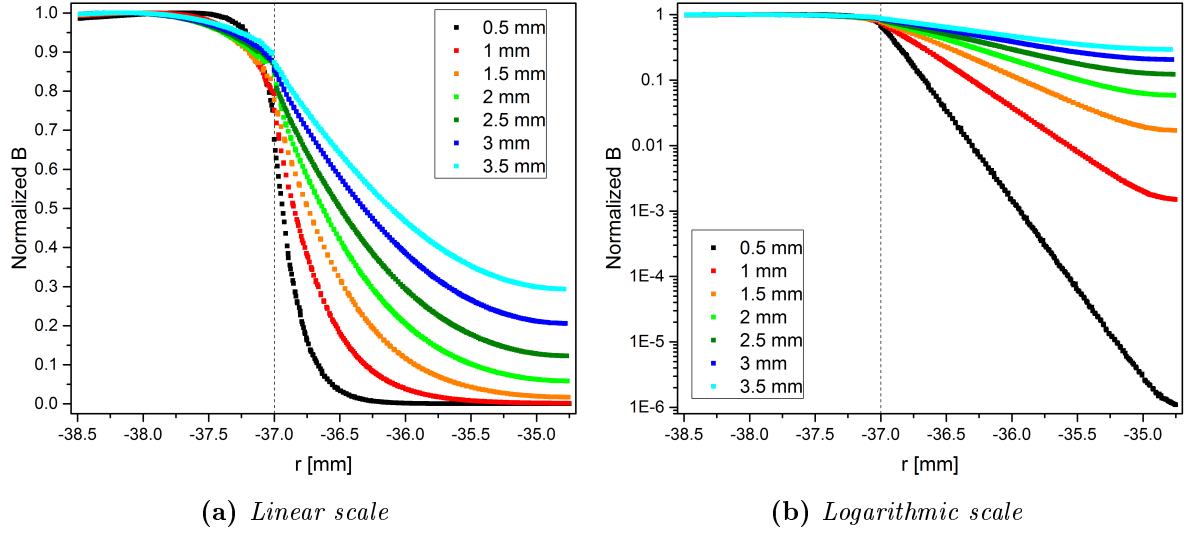


Figure 4.12: Normalized magnetic field in a limited gap for different values of gap width. The entrance of the gap is highlighted by a dashed line.

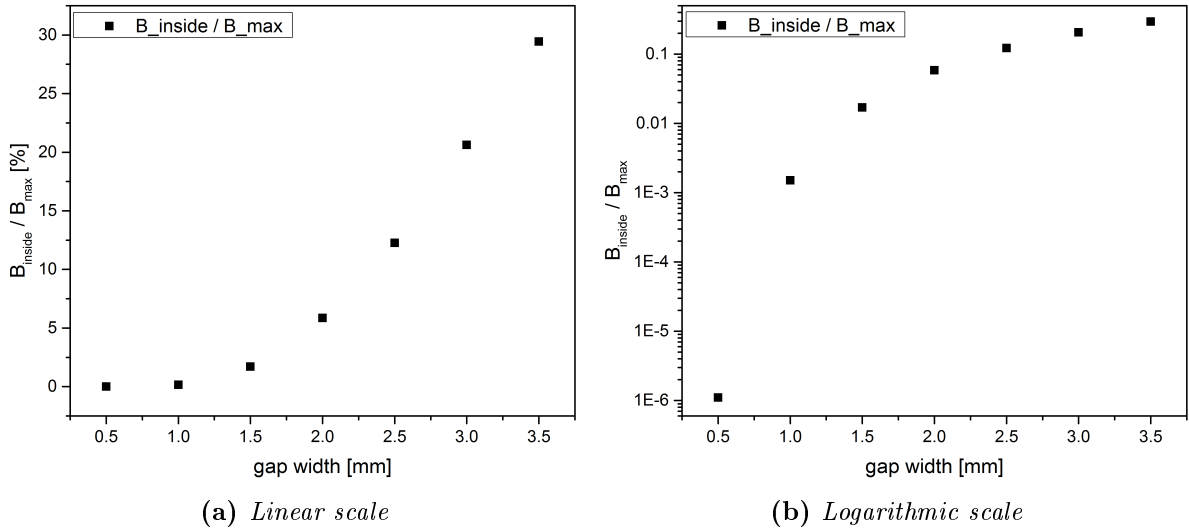


Figure 4.13: Ratio of magnetic field at innermost point of the gap to the maximum value (outside of gap).

5 Construction and Test of a Prototype Chamber

Prior to the production of the niobium chamber a prototype built out of aluminum was investigated, concerning handling, assembly and vacuum issues of the new design.

5.1 Results from Simulations and Design Requirements

The simulations confirm the exponential decay of RF fields propagating into the coaxial structure (see fig. 4.8). Hence operational safety of the new calorimetry chamber is improved by increasing the height of the sample holder, since keeping a location of possible RF heating in a region of low field will suppress any possible disturbance of the measurement process. In contrast to this, thin sample holders are preferred for coating and mechanical handling. In the design process the thickness has to be chosen in a way that both requirements are balanced.

5.1.1 Vacuum and Cleanliness

For operation of the QPR it is essential to maintain a particle free vacuum inside of the resonator, otherwise field emission may occur leading to a quench of the resonator. The vacuum inside of the calorimetry chamber is needed only for thermal insulation. Mounting sensors and equipment inside should be easy and possible outside a clean room. In addition, any screwed connection is a source of metallic particles and cable insulation made out of plastic potentially outgas. All this leads to the requirement of a vacuum leak tight connection between calorimetry chamber and resonator volume. The maximum leak rate allowed is specified to 10^{-7} mbar l/s.

5.1.2 Thermal Conductivity

The measurement principle of the QPR relies on the thermal equilibrium of the sample. In this equilibrium, RF heating, DC heating and conduction cooling to the liquid helium bath are in a steady state. Since the measurement relies on the difference of DC heater power with and without RF ($P_{DC1} - P_{DC2}$), all thermal quantities have to be constant only for the acquisition time of one data point. Since a vacuum tight connection of all parts is required one can assume a sufficiently stable thermal contact to be ensured, the consequence being that no additional restrictions to the thermal connection of the parts have to be made.

5.2 Description of the Design

The design of the new calorimetry chamber consists of three parts: sample, tube and (bottom) flange. Technical drawings are provided in fig. 5.2, 5.3 and 5.4. An exploded view of the calorimetry chamber is depicted in fig. 4.1.

5.2.1 Sample Holder

The most important quantity to be specified first is the total height of the sample holder. It was decided to retain all dimensions unchanged which are relevant for measurements, i. e. placement of central heater and temperature sensors. This defines the minimal height of the sample holder to be 12 mm (see sensor mounting in fig. 5.2). The RF magnetic field strength in the coaxial structure at that position amounts to 2.80 – 4.35 mT (see dashed lines fig. 5.1) – in the common normalization to a peak field on the sample surface of 150 mT. For the simulations presented above, the MFE factor is smaller than 4, for gaps smaller than 500 μm (see sec. 4.5.1). That yields a surface peak field of around 17 mT confined to a sub-mm small region around a sharp edge. Recall the scaling of RF dissipation ($P_{\text{diss}} \propto B^2$), hence a field strength two orders of magnitude lower than on the sample surface on an area of negligible size was accepted. This choice of height provides the further advantage, that, if the sample is coated in a process needing substrate heating, a larger contacting surface to a heating plate is enabled.

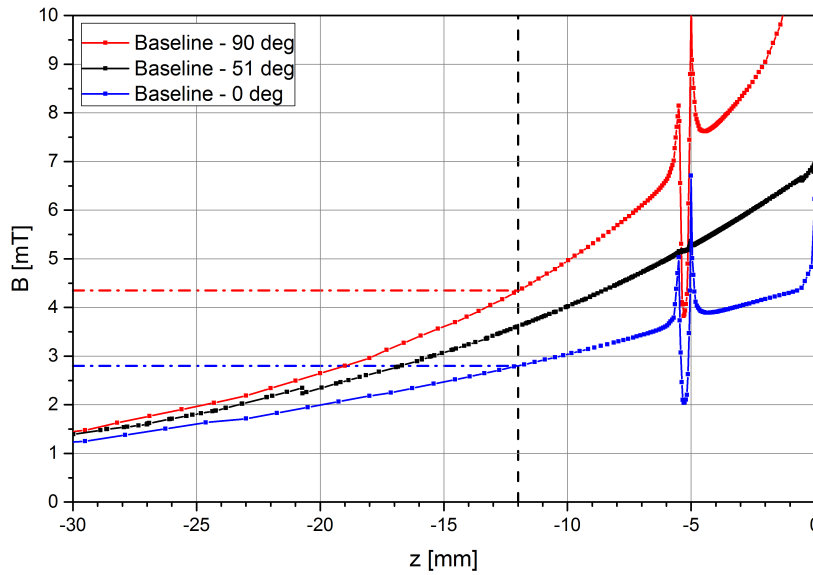


Figure 5.1: Magnetic field in the coaxial structure for the baseline geometry with gap at $z = -5$ mm. The magnetic field to be expected without field enhancement at $z = -12$ mm is highlighted by dashed lines.

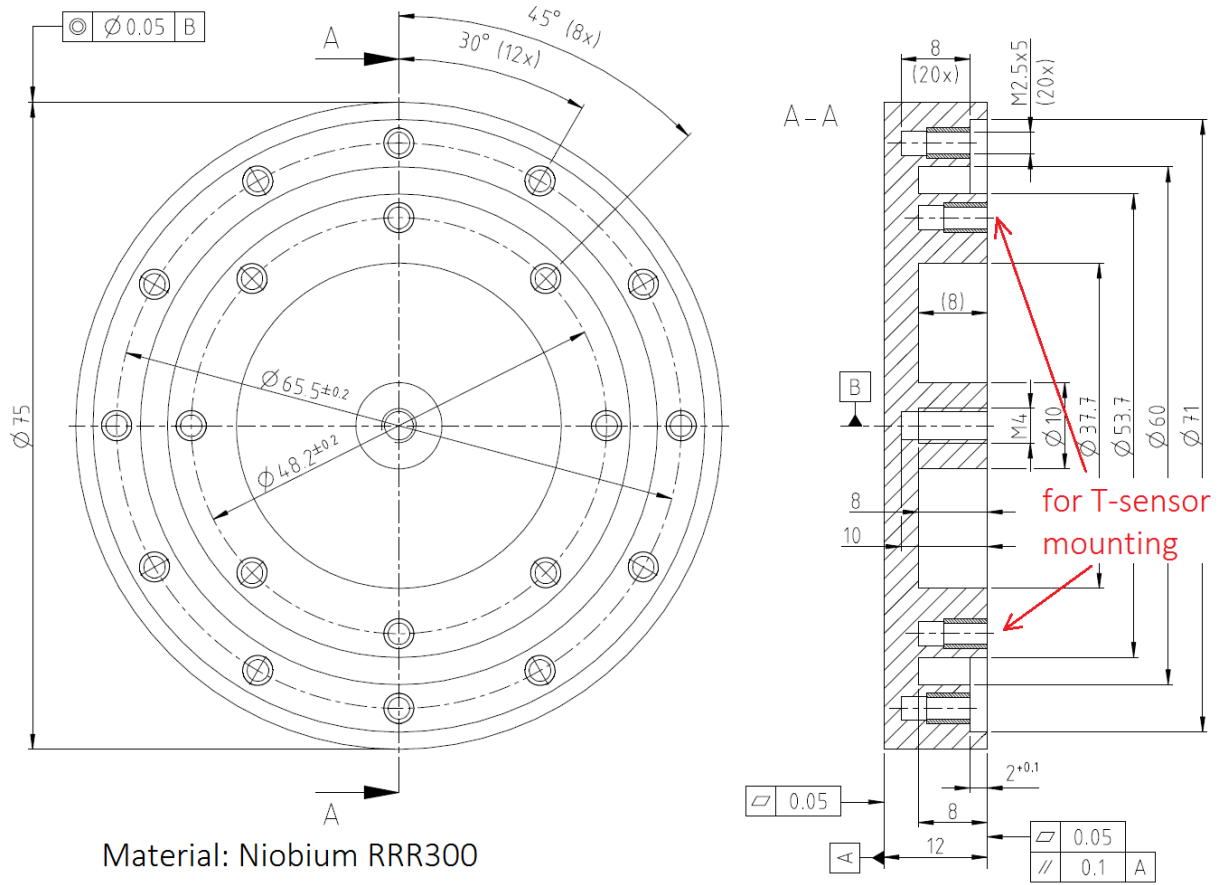


Figure 5.2: Technical drawing of the sample holder: bottom view and cross section.
Property: Reuter Technologie GmbH, Alzenau.

Sample and tube are connected via inlying bolting. The threads inside of the sample holder are placed in a ring separated from the one where the temperature sensors are mounted. This ensures that heat, generated by both DC heater and RF dissipation, is transported on a path similar to the existing sample design. In this way temperature profiles of the different sample holder designs differ as little as possible.

5.2.2 Tube and Bottom Flange

Following the design of the existing calorimetry chamber the tube wall thickness of 2 mm remains unchanged. At the top level of the tube a positive offset of 2 mm is implemented which provides easy positioning and centering of the sample (see fig. 5.3). The mating part to the bolting of the sample is done using open slotted holes in order to vent the threads. At the bottom level of the tube, the wall thickness is increased to include threads for bolting the tube to the flange. These threads are positioned close to the outer edge of the tube to maximize the internal diameter. This

5.2 Description of the Design

is important to provide access to the bottom of the sample for sensor mounting after assembly of the chamber. The threads are open at the top end to ensure proper evacuation.

As bottom flange a CF DN100 blank flange is used and adapted. The total height of the calorimetry chamber for the QPR at HZB and CERN differ by 3.5 mm. By using individual bottom flanges this difference can be compensated and the chamber can be used in both resonators. Hence no additional niobium tube is required, which avoids one source of additional costs and measurement uncertainties.

For the prototype the connections of all parts are built in simple way, especially without dedicated vacuum seals. The leak rate is a subject of tests and starting from this point additional gaskets are designed if required.

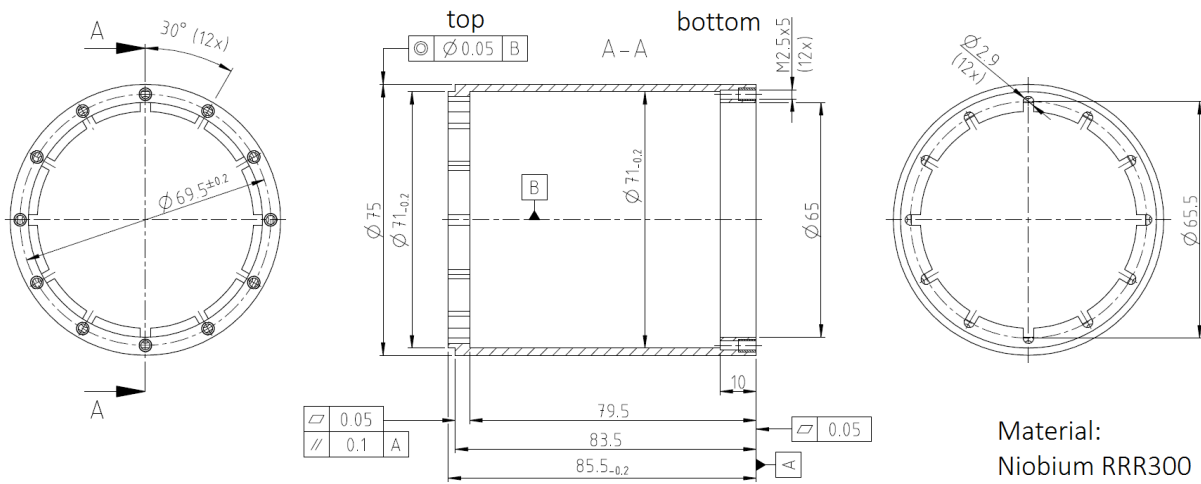


Figure 5.3: Technical drawing of the tube – from left to right: bottom view, cross section, top view. Property: Reuter Technologie GmbH, Alzenau.

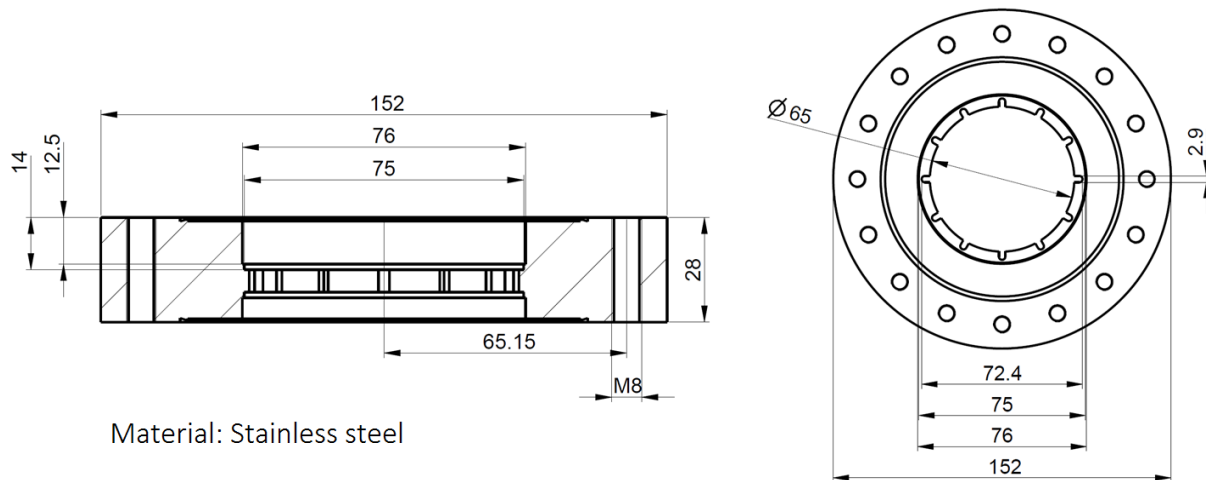


Figure 5.4: Technical drawing of the bottom flange – cross section and top view.

5.3 Vacuum Tests

The cleanliness of the resonator vacuum is a critical aspect of the new design. A dedicated test environment is set up to measure the leak rate of the chamber. The chamber is mounted into a vacuum system consisting of two volumes, representing resonator and insulation vacuum. The system is connected to an ASM 310 leak detector (Pfeiffer Vacuum GmbH) which is a compact device containing a primary vacuum pump, a pressure gauge and a helium leak detector. Using angle valves 1 and 2 both branches can be separated from the pump and from each other. Furthermore a controllable gas inlet is available via two needle leak valves. A sketch of the setup is depicted in figure 5.5.

The minimum pressure achievable by the ASM 310 is around 10^{-4} mbar hence gaskets made out of both copper and flouroelastomers (Viton) can be used.

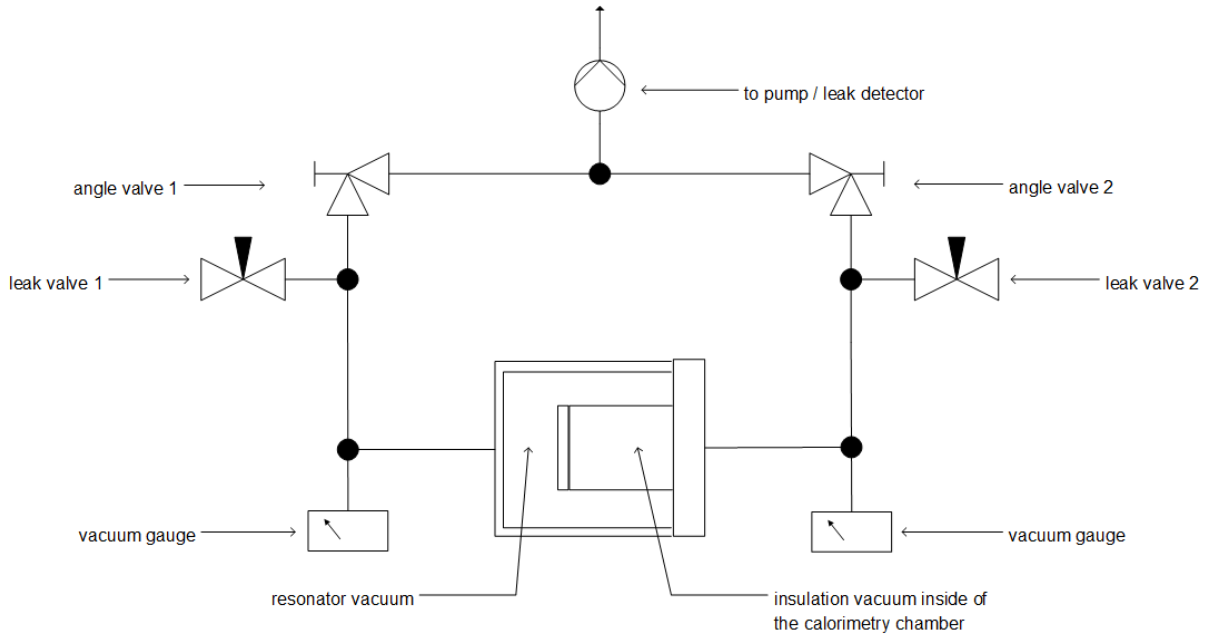


Figure 5.5: *Sketch of the vacuum test setup.*

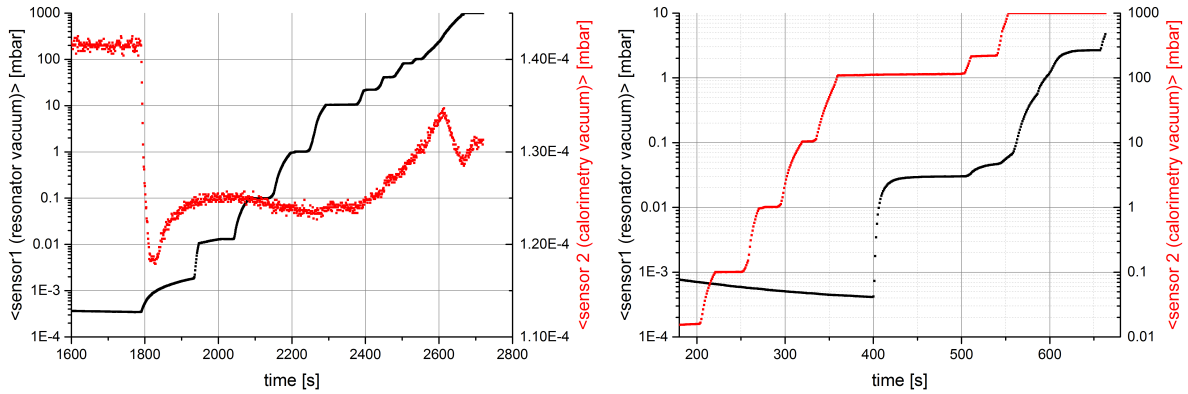
5.3.1 First Tests without Additional Gasket

The aluminum prototype as described in sec. 5.2 was mounted into the vacuum system. All parts of the system were copper-sealed, leading to a leak rate of the vacuum system as a whole to ambient atmosphere smaller than $5 \cdot 10^{-11}$ mbar l/s. Starting from a base pressure smaller than 10^{-3} mbar in both volumes, one angle valve was closed and the related volume was vented slowly with filtered air. This procedure was repeated for both volumes.

5.3 Vacuum Tests

The pressure curves of both measurements are depicted in fig. 5.6. It is visible that venting the insulation vacuum caused a higher leak rate than vice versa. This can be explained by forces pushing apart sample and tube instead of holding them together in case of venting the resonator. Since filtered air was used for venting, instead of helium, the leak detector was not able to quantify a leak rate. From the measured pressure curves, leak rates greater than 10^{-6} mbar l/s can be derived which is far above the specification.

This measurement had two consequences: First, the tightness had to be improved which was done using an indium wire gasket in between the parts of the chamber. Second, operational safety of the calorimetry chamber was improved by using a pumping procedure in which the insulation vacuum was pumped prior to the resonator vacuum and vented after.



(a) Gas inlet into resonator vacuum. At $t = 1800$ s the angle valve to the resonator vacuum is closed leading to a pressure drop in the remaining volume.

(b) Gas inlet into insulation vacuum. The strong increase of resonator pressure at $t \approx 400$ s points to an possibly unstable connection of the chamber.

Figure 5.6: Leak test of the aluminum prototype chamber without additional gasket.

5.3.2 Measurements with Indium Gasket

In order to improve the leak rate a gasket using indium wire was implemented. For prototype tests wire of diameter 0.5 mm was used. It was pressed in between the matching surfaces of sample, tube and bottom flange. The vacuum system was partly sealed using flouroelastomers (Viton) yielding a total leak rate to ambient atmosphere of $2.8 \cdot 10^{-9}$ mbar l/s. Both branches of the system were evacuated and after closing angle valve 1 the resonator volume was vented with helium gas. No deviation in leak rate was observed which proves a tightness of the indium gasket better than 10^{-10} mbar l/s.

After disassembly, the thickness of the pressed indium wire was measured using a micrometer caliper. Values between 0.20 and 0.23 mm were obtained. In order to avoid a circumferential gap between sample and tube, the wire volume has to be taken into account for the final design of the chamber made out of niobium.

6 Design and Production of the Niobium Chamber

6.1 Design Changes due to Aluminum Prototype Tests

6.1.1 Implementation of an Indium Wire Gasket

Measurements and tests with the aluminum prototype chamber revealed the necessity of an additional gasket in order to achieve a leak tight connection of all parts. It has been decided to use indium wire for this purpose. Indium has suitable mechanical properties since it is very malleable and provides low outgassing. It becomes superconducting below $T_c = 3.41$ K and has a critical magnetic field of $B_c = 28.6$ mT [50, 51]. Both quantities are significantly smaller than the ones of niobium ($B_{sh} \approx 230$ mT and $T_c = 9.25$ K [12, 23]), hence it has to be ensured that indium does not contribute to the RF surface inside the coaxial structure. Otherwise significant RF heating may occur, disturbing the measurement.

The connection of niobium tube and bottom flange can remain unchanged since RF effects are negligible at this location and no large magnetic field is present. As in the prototype design a closed loop of indium wire is pressed in between of the contacting surfaces of tube and flange. At the connection of sample and tube the indium wire gasket is hidden in a small chamfer (see fig. 6.1). The resulting hollow space is dimensioned to include 90 % of a wire which is 0.5 mm in diameter. The remaining 10 % are intended to compensate for possible flatness imperfections without causing any disturbing gap between sample and tube.

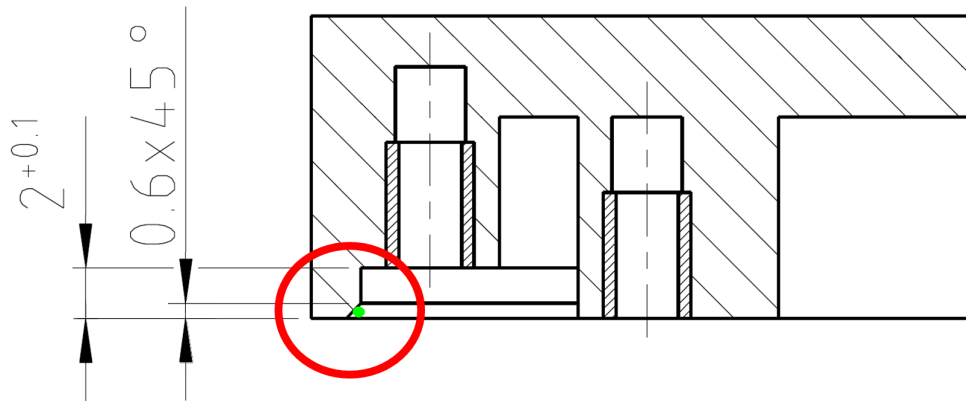


Figure 6.1: Implementation of an indium wire gasket. The wire is illustrated by a green dot. Property: Reuter Technologie GmbH, Alzenau.

6.1 Design Changes due to Aluminum Prototype Tests

The indium wire in between of tube and bottom flange increases the total height of the calorimetry chamber. This offset has to be compensated since the distance between sample surface and quadrupole pole shoes amounts to only 0.5 mm in the HZB design. Measurements of the indium gasket thickness at the prototype yield values of about 0.2 mm. In order to compensate for this and to implement a safety margin for both gaskets, the recess inside the bottom flange is deepened by 0.5 mm. A section view, illustrating this compensation and the different lengths of coaxial structure for the QPR at CERN and HZB is given in fig. 6.2.

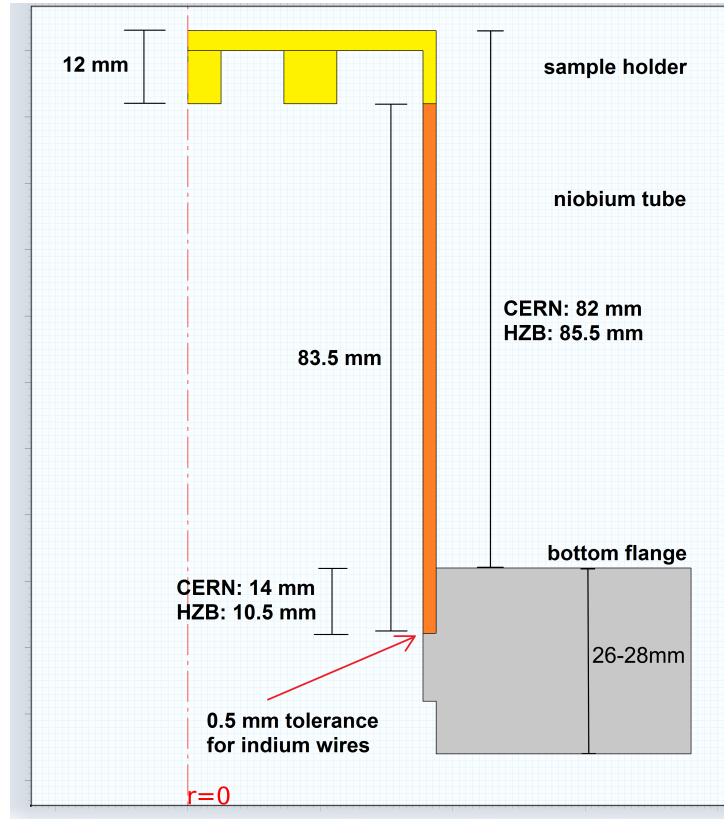


Figure 6.2: Cross section of the calorimetry chamber. The difference in length of coaxial structure, comparing the QPR at CERN and HZB, is compensated using different bottom flanges.

6.1.2 Modification of the Bolting

All parts of the calorimetry chamber are connected via inlying bolting as in the prototype design. Due to the malleability of niobium helical screw thread inserts are used instead of niobium threads. The inserts are made out of CuSn6 which is a (non-magnetic) copper tin alloy (bronze) with 6 % tin content. The screws used are out of titanium which is also non-magnetic and its integral thermal contraction for a cool-down from room temperature to about 2 K is nearly the same as the one of niobium.

During production of the niobium parts difficulties in implementing helical screw thread inserts in the niobium tube emerged. It has been decided to laser weld tapped bushings made out of titanium grade 2 instead. Due to the greater high-temperature resistance of titanium – compared to bronze – this solution is also applied to the sample holder. This high-temperature resistance is useful for bake-out procedures and coatings requiring substrate heating.

6.1.3 Geometric Dimensioning and Tolerancing

The geometric dimensioning and tolerancing described in this section relates only to the parts made out of niobium and is the same for both parts. The bottom flange (stainless steel) is manufactured in-house and adapted to the niobium parts.

The operation of the QPR requires intact superconducting RF surfaces, parallelism of sample surface and quadrupole pole shoes and concentricity of the coaxial structure. Therefore parallelism of all horizontal surfaces of 0.1 mm is specified. In addition, the flatness of these surfaces has to be smaller than 0.05 mm. As concentricity of the outer cylinder surfaces 0.05 mm is specified (see fig. 5.2 and 5.3). A limit on the surface roughness quantity R_z is set to 10 μm for all surfaces.

6.2 Production and Surface Treatment

The niobium parts were manufactured by REUTER TECHNOLOGIE GmbH, Alzenau, from large grain ingot niobium, RRR 300. Both parts were milled from a solid cylinder. In order to prepare the first RF measurement, several steps of surface treatments had to be performed:

Ultrasonic Bath First all parts were cleaned to remove grease and other easy removable remnants from the production procedure. This was done in a cleanroom using two ultrasonic baths with cleaning agent (Tickopur 3) and ultrapure water sequentially.

Buffered Chemical Polishing (BCP) It is known that after manufacture the surface layers of niobium are damaged and contaminated, which has big impact on the RF properties. In order to restore an intact surface and to further remove impurities a Buffered Chemical Polishing (BCP) is performed. During the so-called bulk-BCP of the sample holder 150 μm were removed. The RF properties of the tube are less important, hence only 40 μm were etched. BCP uses HF , HNO_3 and H_3PO_4 with a volume ratio of 1:1:2, the temperature of the acid mixture is kept below 18° in order to avoid polluting the niobium with hydrogen [12].

6.3 Leak Rate Measurements

High Pressure Rinse (HPR) After assembly of the chamber and successful leak tests (see sec. 6.3) a High Pressure Rinse (HPR) constituted the last step of surface treatments before mounting into the QPR. In a cleanroom the chamber was rinsed in a two-step process using ultrapure water first and ethanol afterwards. By rinsing, all dust particles present on the surfaces were removed to maintain a particle free vacuum inside the resonator. Using ethanol in the second step improved drying. After rinsing the chamber it was wrapped up in plastic foil and transferred to mounting into the resonator.

6.3 Leak Rate Measurements

After chemical polishing the chamber was assembled and vacuum leak tested. The vacuum tests were performed using the same setup as with the aluminum prototype. The following, standardized procedure was applied: Using the helium leak detector ASM 310, the whole vacuum system was evacuated, yielding the total leak rate of the system to ambient atmosphere. Afterwards the resonator volume was disconnected from the pump by closing angle valve 1 (see fig. 5.5) and vented with helium gas up to atmospheric pressure. The maximum leak rate observed by the leak detector was noted.

6.3.1 Measurements at Room Temperature

The chamfer at the bottom level of the sample is dimensioned to include an indium wire gasket which is 0.5 mm in diameter (see sec. 6.1.1). At the connection of tube and bottom flange the same type of wire was used. A leak rate of $4 \cdot 10^{-4}$ mbar l/s was measured. Disassembly and optical inspection revealed issues at both gaskets: At the connection of sample and tube the indium wire was swaged to a triangular cross-section not filling the chamfer completely. In the design of the chamfer, the impact of the chemical polishing on the dimensions of the chamfer had been neglected. Assuming uniform etching of all surfaces, the indium volume required to fill the chamfer increases by 50 %.

During manufacture of the bottom flange, an additional relief groove had to be implemented inside the recess hosting the niobium tube. The indium wire used could not fill this additional volume, too.

In a new measurement indium wire of 1 mm diameter was used for both gaskets. The vacuum test system was copper-sealed with a total leak rate to ambient atmosphere of $6 \cdot 10^{-10}$ mbar l/s. No change of leak rate was detected on any helium inlet into the resonator volume, indicating a total leak rate of both indium gaskets smaller than $1 \cdot 10^{-10}$ mbar l/s. Drawback of this choice of diameter was a circumferential gap resulting in between of sample and tube. The height of this gap could not be measured precisely, but using a caliper gauge a value of about 0.2 – 0.3 mm was estimated.

6.3.2 Thermal Cycles and Tests at Cryogenic Temperatures

To investigate the leak rate at cryogenic temperatures, the calorimetry chamber was cooled down while being connected to the vacuum system. Therefore, the bottom part of the system was immersed in liquid nitrogen. Since the two-sided bottom flange of the calorimetry chamber was used for mounting into the system, the conduction cooling to the liquid nitrogen bath was similar to the operational conditions when mounted on the QPR. The sample was equipped with PT1000 resistance temperature detectors. Before cool-down the vacuum system was evacuated. After having reached the base pressure, angle valve 1 was closed and the resonator volume was filled with helium enriched atmosphere. With this procedure any leak occurring due to cooling down the chamber could be detected immediately by the helium leak detector.

The same indium gasket as for the last test at room temperature was used, i. e. the chamber had not been dismantled. At room temperature a base leak rate of $2 \cdot 10^{-10}$ mbar l/s was measured. Cooling down below 260 K caused the leak rate to suddenly increase above 10^{-8} mbar l/s. At 80 K the leak rate stabilized at $1.2 \cdot 10^{-6}$ mbar l/s.

After warm-up all screws inside the calorimetry chamber were retightened. Subsequently the bare calorimetry chamber was cycled thermally by immersing into liquid nitrogen. After retightening all screws again, both measurements, at room temperature and using liquid nitrogen, were repeated. In both measurements no change of leak rate was detected on any helium inlet into the resonator volume. During the cold test a total leak rate of $6.1 \cdot 10^{-11}$ mbar l/s was measured at 85 K sample temperature. This indium gasket fulfilled the requirements and was used for the first RF test of the calorimetry chamber (see sec. 7). Cooling down to 1.6 K during the RF test using liquid helium did not reveal any suspicious performance of the gaskets.

7 First RF Measurements

In this chapter the first RF measurement of the new calorimetry chamber using the Quadrupole Resonator at CERN is described. After successful vacuum leak test at liquid nitrogen temperature (see sec. 6.3) the chamber was shipped to CERN. At CERN, a 5 bar rinse was performed using ultrapure water and ethanol, constituting the last step of surface treatments before mounting into the QPR (see sec. 6.2).

7.1 Measurement Setup

For temperature measurement, six diode temperature sensors (Lake Shore Cryotronics, Inc.) were used. Four of them were screwed to the bottom of the sample as intended for common QPR operation (see fig. 5.2). In order to obtain additional sensitivity on temperature profiles, the niobium tube was equipped with two sensors. They were mounted on copper blocks which were glued closely below the joint between sample holder and the tube. These sensors were intended to monitor possible RF heating at the indium gasket. Unfortunately only one calibrated diode was available which was placed at the sample, below a region of high magnetic field. Unless stated explicitly, in the following all temperature values given refer to the calibrated diode (Diode A).

A DC heater was mounted as required by the calorimetric measurement principle (see sec. 3.2). Furthermore a single axis fluxgate magnetometer (Bartington Instruments Ltd.) was attached to the inside wall of the tube. Due to its orientation the vertical component of the magnetic field (perpendicular to the sample surface) was measured.

7.1.1 Resonant Frequency and Height of Calorimetry Chamber

The resonant frequency of the quadrupole mode is sensitive to the distance between sample surface and quadrupole rods. This is used to estimate the thickness of the indium gaskets. The QPR at CERN is optimized to 400 MHz at a gap of 1 mm [34]. Simulations yield that increasing this distance by 0.4 mm lowers the resonant frequency by 2.4 MHz [52]. A resonant frequency of 397.916 MHz was measured. Scaling the value obtained from simulations yields an increase of the gap by 350 μm . Now the total thickness of both indium gaskets can be estimated: The bottom flange was designed to provide an additional offset of 0.5 mm for safety reasons (see sec. 6.1.1). Due to BCP the gap is increased further by 340 μm (see sec. 6.2). Adding up and comparing to the measured value of 350 μm yields a vertical offset due to both indium gaskets of 490 μm .

7.2 Superconducting Properties

During initial cool-down of the resonator, the superconducting transition temperature of the calorimetry chamber can be observed using the fluxgate magnetometer. Due to the Meissner effect, the magnetic flux penetrating niobium is expelled for temperatures $T < T_c$ (see sec. 2.2). At the transition temperature a jump-like change of measured magnetic field is expected.

The magnetic flux measured by the fluxgate magnetometer and the temperature of the sample, obtained from the calibrated sensor are shown in fig. 7.1. A transition temperature of 9.35–9.20 K as visible in fig. 7.1b is in good agreement with the literature value of $T_c = 9.25$ K [23]. Note that due to the cooling rate, the dynamic measurement uncertainty on temperature amounts to about 0.1 K, since the data acquisition rate is approximately one point per second.

The jump-like changes of magnetic field at higher temperature ($T \approx 120$ K, see fig. 7.1a) are not understood so far. Possibly the superconducting transitions of the quadrupole rods are visible here.

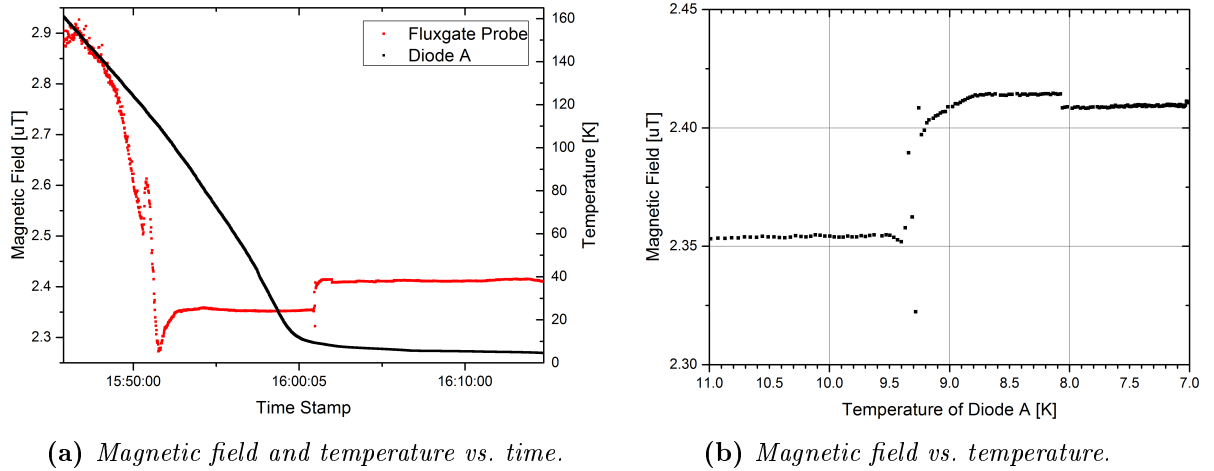


Figure 7.1: Magnetic field and temperature observed during initial cool-down.

7.2.1 Surface Resistance

The main goal of the RF measurement was the surface resistance characterization of the new calorimetry chamber. The surface resistance was measured in two settings, at constant temperature with varying RF magnetic field (see fig. 7.2) and vice versa (fig. 7.3).

The results from measuring at **constant temperature** are shown in fig. 7.2. The large values of R_s and the strong dependence on magnetic field strength are fully unexpected for a sample made of niobium.

Measuring at constant temperature, the maximum magnetic field reachable is defined by RF heating of the sample. This is given, when the temperature of interest is achieved with RF

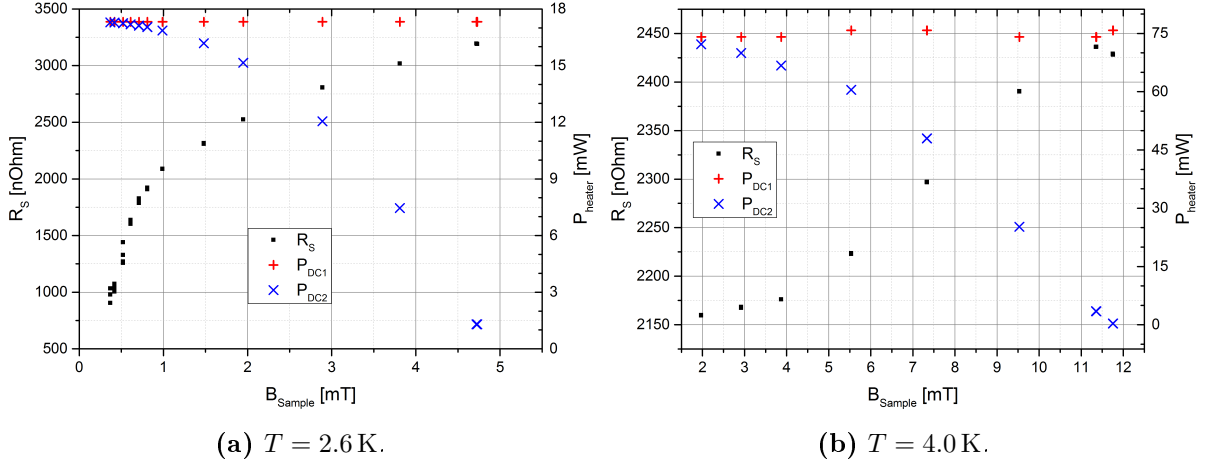


Figure 7.2: Surface resistance measurement at constant temperature.

dissipation only ($P_{\text{DC2}} \rightarrow 0$, i. e. the heater is switched off).

The minimum field is defined by RF measurement boundary conditions. The resonant frequency of the QPR is very sensitive to changes in ambient conditions and due to the bandwidth of the QPR of few hundred Hz, continuous adjustment is required. A PLL is used in order to keep track of the resonance frequency, hence a non-zero field level is required for feed-back. Furthermore, a weakly coupled field probe is used, limiting the measurement resolution at low field. As shown below, the uncertainty in R_s is estimated to be at least 50 % at low field. Nevertheless, a significant increase of surface resistance with increasing RF field is observed, which cannot be explained by BCS theory (see sec. 2.2). Using eq. 2.25 the surface resistance expected from BCS is calculated for the operation frequency of 400 MHz:

$$R_{s, \text{BCS}} (2.6 \text{ K}) \approx 6 \text{ n}\Omega$$

$$R_{s, \text{BCS}} (4.0 \text{ K}) \approx 43 \text{ n}\Omega$$

Especially at 2.6 K residual surface resistance may not be neglected. However, typical values of less than $100 \text{ n}\Omega$ [12] cannot explain the measurement results.

The results from measuring at **constant RF field** are depicted in fig. 7.3. The minimum temperature of interest achievable is limited by RF heating of the sample.

Typically measurements with the CERN QPR are performed with at least several mT of magnetic field [52]. When measuring at constant field of 0.5 mT, data was taken multiple times at 2.6 K (see fig. 7.3a). From the spread observed here, the uncertainty in R_s is estimated to be at least 50 %. Note that RF dissipation scales proportional to $(B_{\text{sample}})^2$ (see eq. 2.4), hence the difference between P_{DC1} and P_{DC2} is too little to be visible in fig. 7.3a.

The results obtained at 5 mT show several unexpected aspects (see fig. 7.3b). Starting at 2.6 K with an approximately constant surface resistance of $3170 \text{ n}\Omega$, the resistance increases by $300 \text{ n}\Omega$

7.2 Superconducting Properties

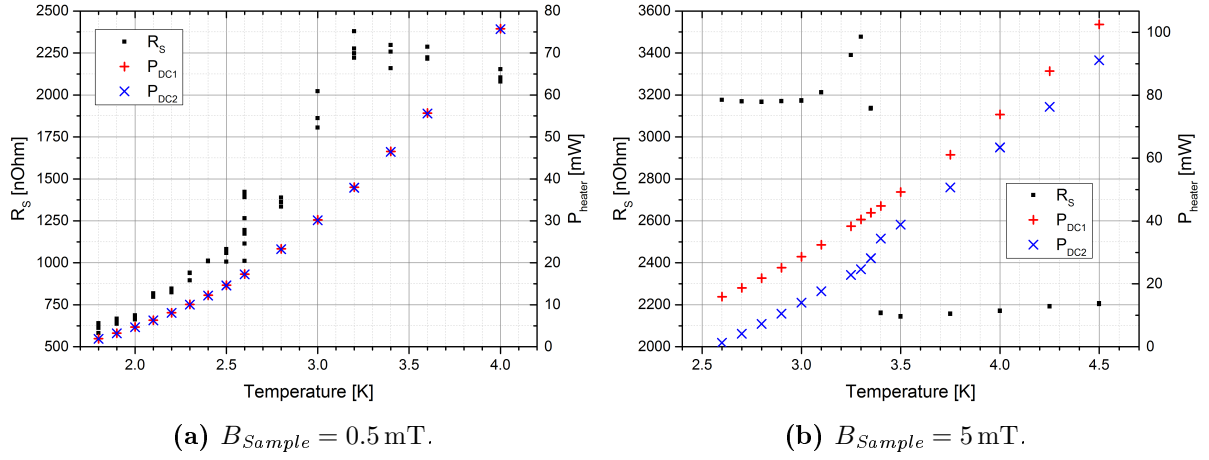


Figure 7.3: Surface resistance measurement at constant RF field.

in the interval from 3.0 K to 3.3 K. Within 100 mK a steep decrease by 40 % is observed. From 3.5 K to 4.5 K the surface resistance increases by 60 n Ω .

Regarding the critical temperature of indium ($T_c = 3.41 \text{ K}$ [50]), the higher resistance below 3.3 K can be explained qualitatively by direct RF losses in the circumferential gap at the upper vacuum seal (see sec. 6.3). Approaching T_c , the critical field of goes to zero, leading to a quench of indium even at low magnetic field.

The abrupt decrease of surface resistance above 3.4 K is caused by a reduction of RF dissipation as clearly visible from P_{DC2} . This cannot be explained by the surface resistance of indium. Above 3.4 K normal conducting indium would lead to a contribution of RF dissipation, approximately independent on temperature. A possible impact of changing thermal properties of indium can be excluded, since no phase transition is observed in DC heater power with RF switched off (P_{DC1}).

Between 3.5 K and 4.5 K the surface resistance increases by 60 n Ω . This increase is close to the value expected for niobium. At 400 MHz the BCS approximation formula yields an increase of 35 n Ω in this temperature range (see eq. 2.25).

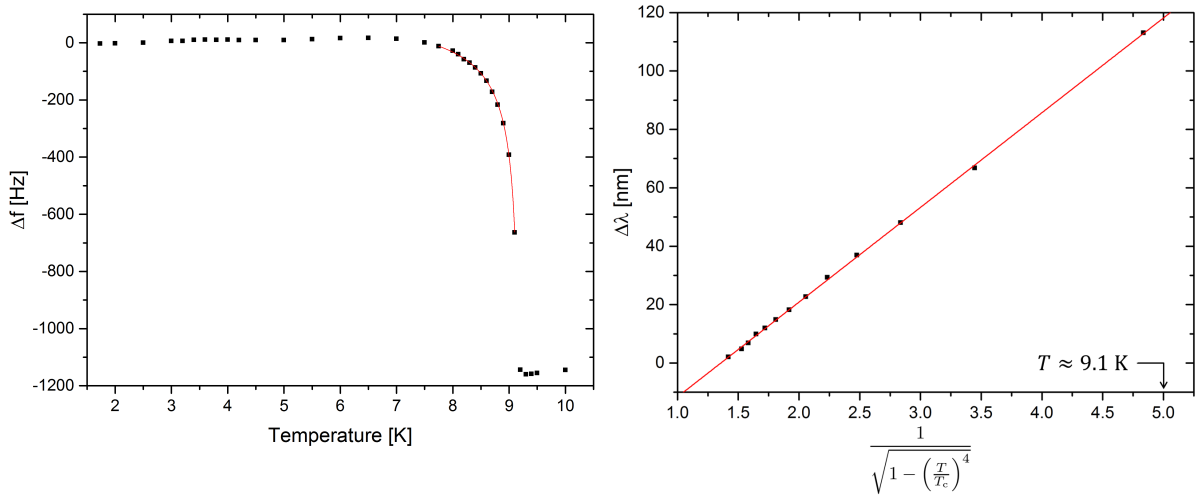
7.2.2 Penetration Depth and RRR

The RF penetration depth is determined employing the shift of resonant frequency while heating the sample (see sec. 3.3). The resonant frequency is measured using a vector network analyzer which provides precision measurements at low RF levels. Above 7.5 K a significant shift is observed as visible in fig. 7.4a. According to eq. 3.13 the change of penetration depth is calculated and a fit is performed in the interval between 7.75 K and 9.1 K. Penetration depth and critical temperature are fitted in one step. The fit yields $\lambda_0 = 32.7 \pm 0.3$ nm and $T_c = 9.200 \pm 0.004$ K. From λ_0 mean free path ℓ and RRR are derived using eq. 3.15 and eq. 3.14

$$\ell = 1945_{-1140} \text{ nm}$$

$$\text{RRR} = 720_{-420}$$

with $\lambda_L = 32$ nm and $\xi_0 = 39$ nm taken from literature [40]. The uncertainties for mean free path and RRR are estimated by evaluating the upper and lower limit of λ_0 . Within its uncertainty, the value obtained for λ_0 is compatible with λ_L . Since eq. 3.14 is divergent for $\lambda_0 = \lambda_L$, no upper boundary can be given for ℓ and RRR.



(a) Measured shift of resonant frequency vs. temperature and fit of $\Delta \lambda$ in the range 7.75–9.1 K. (b) Linear representation of the fit, λ_0 is given by the slope of the line. $\Delta \lambda$ was calculated using the data in (a) and eq. 3.13.

Figure 7.4: Penetration depth measurement.

Additionally, the method of determining RRR via the loaded quality factor of the QPR with normal conducting sample is employed. The sample is heated to 13 K in order to ensure the normal conducting state. Using the network analyzer the loaded quality factor of the resonator is measured in transmission. In the normal conducting state Q_{Sample} dominates both Q_0 and Q_e and the resonator becomes undercoupled. Using eq. 3.17, Q_{Sample} is calculated and from this the

7.2 Superconducting Properties

normal conducting surface resistance is obtained (eq. 3.12). The measurement is performed at three quadrupole modes, the results are reported in table 7.1.

For highly pure niobium the transition from normal skin effect to the anomalous skin effect is expected. In addition to the RRR as expected from the normal skin effect (see. eq. 3.18), the parameter α_s (calculated for RRR=300) and the surface resistance in the anomalous limit ($\alpha_s \rightarrow \infty$) are given for all three frequencies.

The normal skin effect is fully valid for $\alpha_s \leq 0.016$, which is only given for a frequency of 400 MHz and $\text{RRR} \leq 50$. For comparison with the mean free path as derived above, the skin depth δ assuming RRR=300 is also given in table 7.1.

Frequency [MHz]	$R_{S, \text{meas.}}$ [m Ω]	$R_{S, \text{anom.}}$ [m Ω]	α_s (RRR300)	$\text{RRR}_{\text{skin eff.}}$	δ_{RRR300} [nm]
397.92	0.613	0.519	3.05	635	570
796.57	0.836	0.824	6.1	680	400
1201.7	1.095	1.084	9.2	600	330

Table 7.1: *RRR from normal conducting Q measurement.*

The values for the surface resistance obtained from measurement are above the ones, calculated in the anomalous limit. This is expected in case of a non-negligible contribution by the normal skin effect. The deviation from the anomalous limit at 400 MHz amounts to 15 % and less than 2 % at higher frequencies. For this reason values for RRR calculated using the normal skin effect are not valid. Nevertheless the good agreement with the anomalous limit indicates a RRR larger than 300 (as measured with the London Penetration depth), since α_s with RRR=300 suggests a higher contribution of the normal skin effect [12].

7.3 Thermal Properties

In this section measurements on temperature profiles and on the thermal conductivity of the calorimetry chamber are discussed.

7.3.1 Temperature Profiles

By comparing temperature profiles obtained from DC heating and RF dissipation, possible RF heating of the indium gasket is investigated. Since only one calibrated temperature sensor was available, a normalization procedure is applied to all five uncalibrated sensors. That enables comparability of all sensor readings to each other. Applying this normalization to data taken with increasing RF magnetic field, no heating of the indium gasket is detected.

Fig. 7.5 shows the temperature readings of all sensors for different DC heater power in thermal equilibrium. Deviations among the sensors are expected since only one sensor is calibrated (Diode A). Sensors C3 and C4 are mounted below the bolting of sample and tube, hence different data is expected due to the temperature profile of the calorimetry chamber (see sec. 7.1). Note, that only temperatures above 1 K could be measured, 1 K corresponds to underrange read-out (see e. g. Diode C3 for $P_{\text{heater}} < 60$ mW).

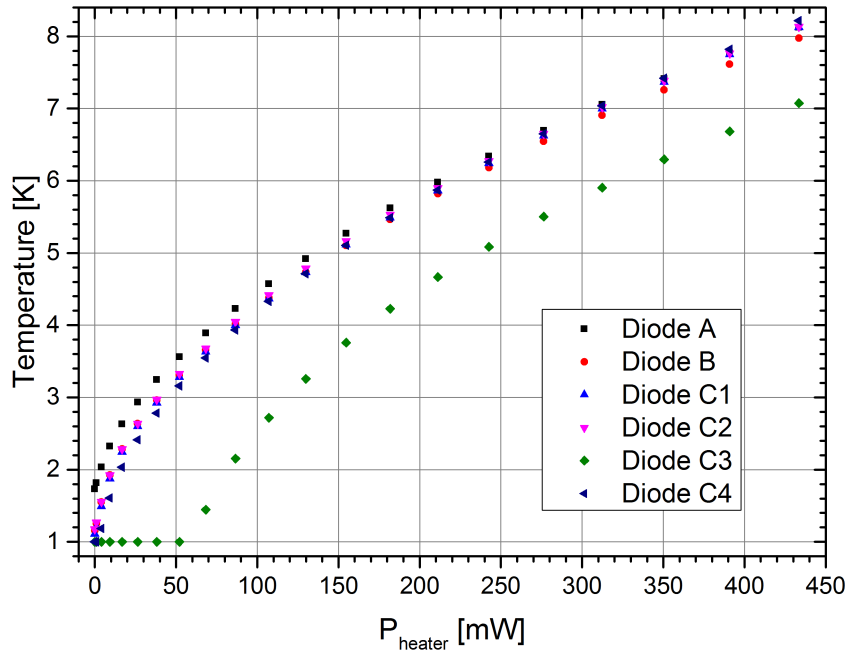


Figure 7.5: Temperature vs. DC heater power. $T = 1$ K denotes underrange read-out.

7.3 Thermal Properties

In order to compare temperature profiles from DC heating and RF dissipation – despite only one calibrated sensor – a normalization procedure is applied to all five uncalibrated sensors: The difference in sensor read-out compared to diode A is plotted and fitted as shown in fig. 7.6a. An exponential or the sum of two exponential functions is convenient to describe the measured data. These functions are no theoretical assumption or expectation, only a good approximation by an analytical expression is needed in order to calculate intermediate values. The residua, remaining after subtracting the normalization from the sensor readings, are plotted in fig. 7.6b.

Next the DC heater was switched off and the sample was heated only by RF dissipation. The temperature data without normalization is shown in fig. 7.7a. A “plateau” is visible in the range of 7 – 9 mT. This is in good agreement with the measured surface resistance, since at $T = 3.4$ K (Diode A) an abrupt decrease of surface resistance was observed (see fig. 7.3b).

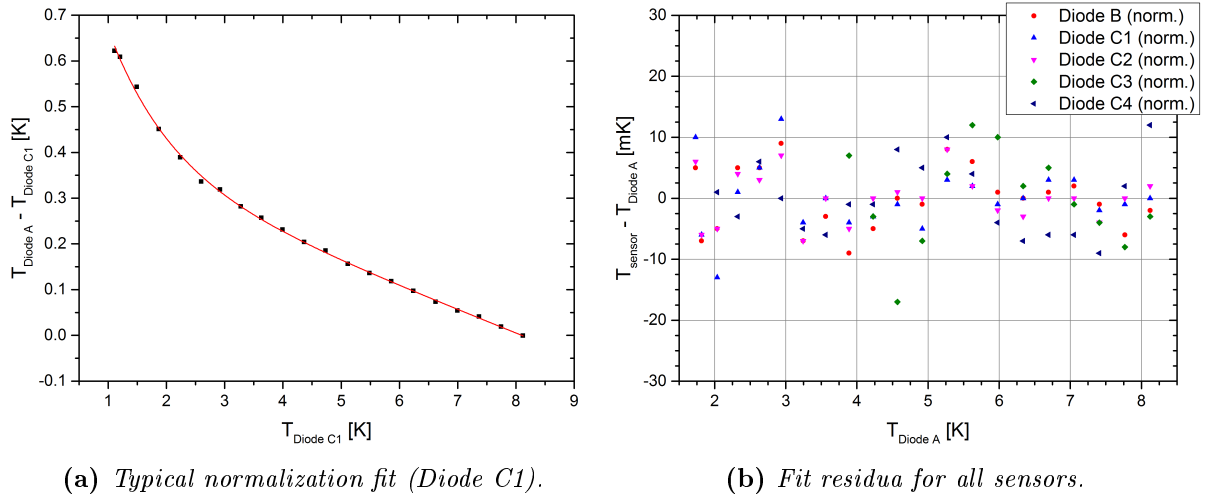


Figure 7.6: Normalization of temperature sensors.

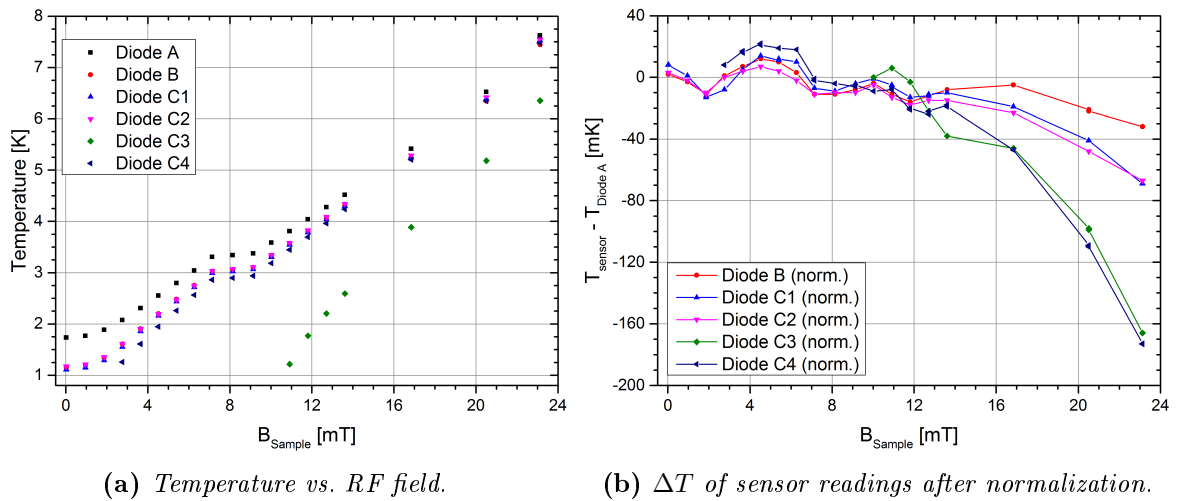


Figure 7.7: RF heating.

That decrease in R_S causes approximately constant RF dissipation, even for increasing magnetic field. Above 9 mT the increasing magnetic field causes the temperature to rise again.

The shape of temperature response to DC and RF heating is consistent as well. Since $P_{\text{diss}} \propto B^2$ a linear rise of temperature with magnetic field corresponds to $\Delta T \propto \sqrt{P}$, which is indeed observed qualitatively for P_{DC} when only the heater is used to produce power P (see fig. 7.5). Note that this relation only holds for constant R_S .

By applying the normalization determined before, the deviation in sensor readings for increasing RF field are obtained as depicted in fig. 7.7b. Note that this is no calibration of the sensors. Especially for diode C3 and C4, mounted on the tube, this normalization results in comparing the temperature profiles caused by DC heating and RF heating. Assuming the uncertainty of the normalization to be 10 mK (see fig. 7.6b), no significant deviation of sensors mounted at the sample is observed below 12 mT. Diode C4 shows slightly higher temperature for 5 mT to 6 mT. Above 12 mT sensors C3 and C4 indicate dominant RF heating of the sample surface. These sensors probe the temperature only at two specific locations, hence RF heating at the indium gasket cannot be excluded. The differences among the sensors mounted on the sample are not understood so far. One possible scenario is given by hot spots on the sample surface causing dominant and localized heating near sensor A.

7.3.2 Thermal Conductivity

Investigating the thermal conductivity of the calorimetry chamber system provides insights on the bulk-RRR of the system and on possible thermal resistance of the indium gaskets.

In the present setup, the thermal conductivity of either sample or entire calorimetry chamber could not be measured directly. For this, several calibrated sensors along a thermal path are required [34]. From the data available, an approximation is performed: The temperature detected by the calibrated sensor for different levels of DC heater power is reconstructed using simulations. The uncertainty of the multi-parameter problem is reduced by optimizing the simulations to data in a temperature range as large as possible.

Fig. 7.8 shows the results of these simulations. The scenarios “RRR50” and “RRR300” use a simplified geometry, neglecting bottom flanges and feed-through of the calorimetry chamber. Comparing these simulations to the full geometry (“all flanges”) shows that uncertainties on the thermal conductivity of the bottom flanges have significant impact on the overall temperature profile. The thermal conductivity of niobium RRR50 was measured at CERN [52], all other thermal properties are taken from literature [53,54].

All simulations yield higher temperature at the position of the calibrated sensor than measured. This supports a high value of RRR as obtained from RF measurements, since thermal conductivity is directly proportional to RRR (see eq. 2.28). Note, that in this thermal analysis the

7.3 Thermal Properties

RRR of the bulk material is addressed. In the present case with material thickness ranging from 2 – 12 mm this may deviate from the surface-RRR measured using RF methods.

Regarding the indium gaskets, a poor thermal contact at either of the gaskets can be excluded, since this would entail even higher temperatures at the location of the sensor.

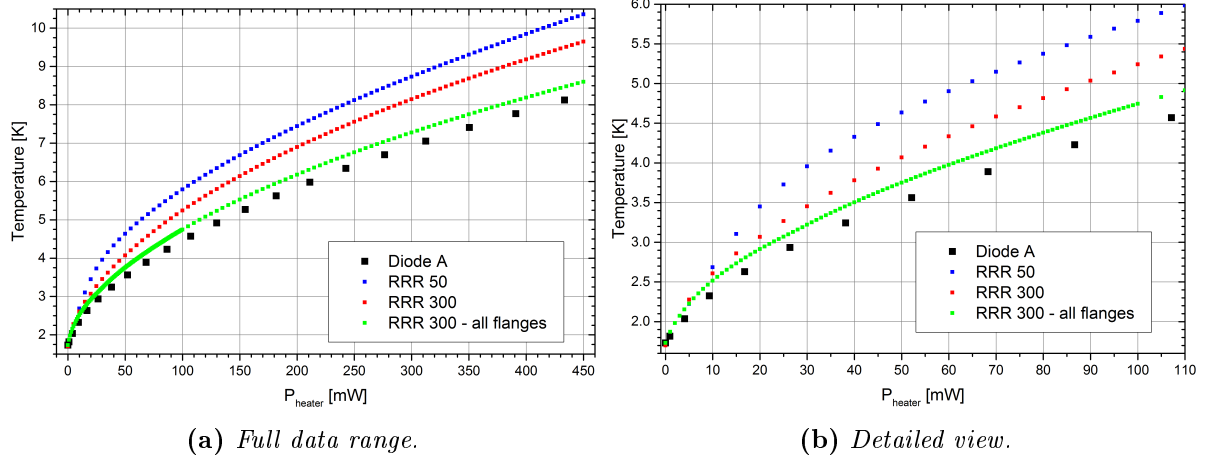


Figure 7.8: Estimation of thermal conductivity using iterative simulations. Measurement results are given by big black squares.

7.4 Further Surface Investigation

After the measurements described above the calorimetry chamber was disassembled. In order to investigate possible reasons for the surface resistance and RRR observed, further tests were performed which are described in this section.

7.4.1 Profilometry

The optical impression of the sample surface after BCP was unexpected, if compared to cavities made of large grain niobium. In order to study the surface structure, a profilometry characterization of different areas was performed using a stylus profiler (Dektak XT™, Bruker Corporation). A stylus with radius $2\text{ }\mu\text{m}$ was used, applying a force of 5 mg to the sample surface. All scans described in the following were performed on a 2 mm long path with 111 nm resolution. A picture of the sample is provided in fig. 7.9, red arrows indicate the location of the scans.

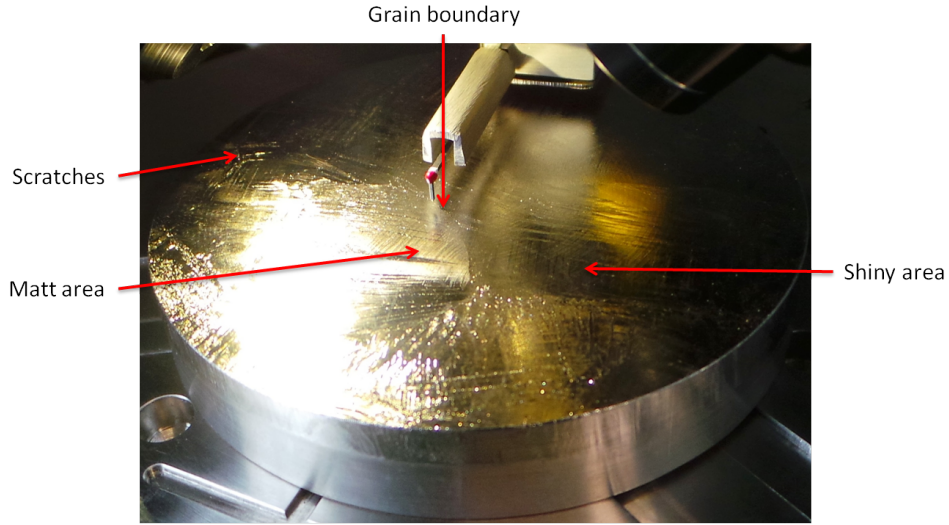
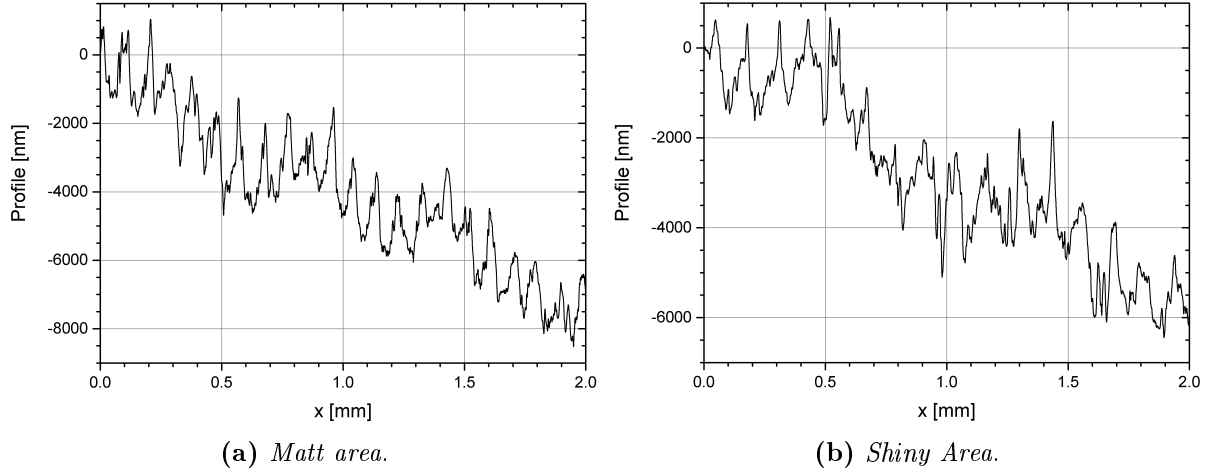
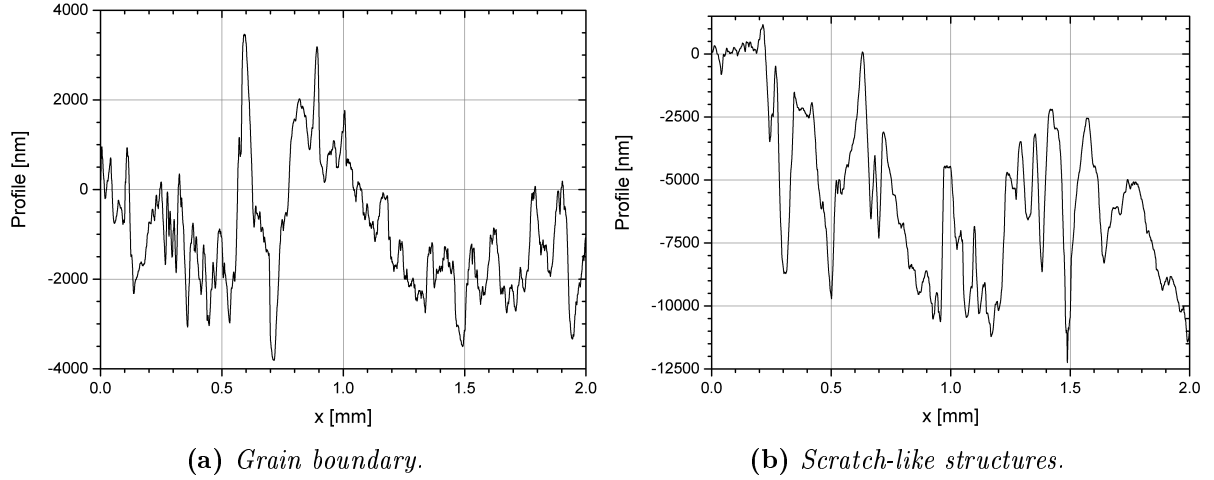


Figure 7.9: Stylus profilometry, red arrows indicate the location of the scans.

The sample surface is mainly occupied by large areas of matt or shiny surface, which are in order of cm^2 . (see fig. A.3). Hence, typical structures of the surface profile are obtained from scans at these locations. Fig. 7.10a and 7.10b show periodic structures with similar height in the range of $2 - 3\text{ }\mu\text{m}$ peak-to-peak. These profiles are probably imprints of the milling, still visible after $150\text{ }\mu\text{m}$ chemical polishing (BCP).

In order to estimate the maximum height of structures present on the sample surface scans on grain boundaries and scratch-like structures were performed. The profiles are depicted in fig. 7.11a and 7.11b. Compared to the results discussed above, these profiles are clearly more irregular and show larger height. The maximum height detected amounts to approximately $11\text{ }\mu\text{m}$.

7.4 Further Surface Investigation

**Figure 7.10:** Results from surface scans on matt and shiny areas.**Figure 7.11:** Results from surface scans at a grain boundary and at scratch-like structures.

Although SRF cavities used for accelerator applications are produced in a very different way [12], the surface roughness of cavities treated with BCP amounts to $5 - 10 \mu\text{m}$ peak-to-peak, which is similar to the one obtained here. For comparison, the results of an investigation using cut-outs from cavities (small grain, high RRR, 1.5 GHz) are shown in figure 7.12. That study revealed the same surface roughness histogram for well and poorly performing cavities and hence excluded the primary contribution of surface roughness to RF dissipation [55].

For this reason surface roughness of the sample surface is excluded to explain the high level of RF surface resistance observed.

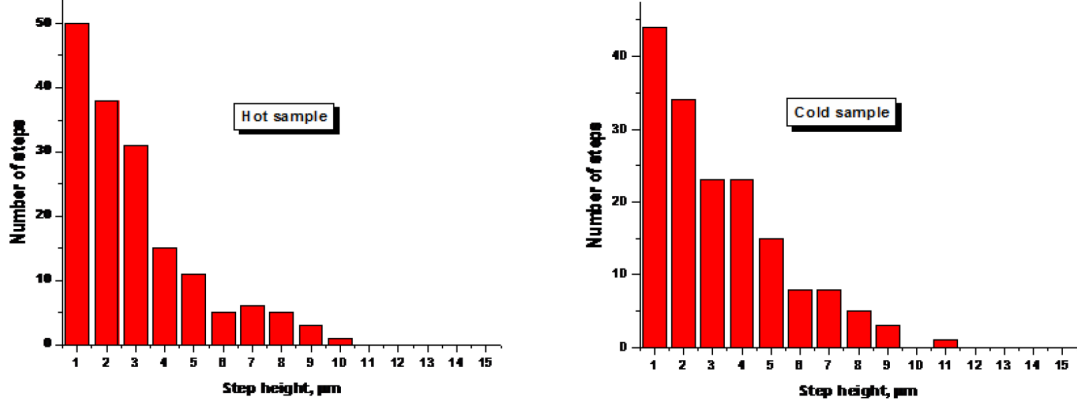


Figure 7.12: Histograms of the step height distributions for hot and cold samples, obtained using white light optical profilometry. The samples are cut-outs from a small grain BCP cavity. Each histogram contains the data from six scans, each spanning 1 cm in length [55].

7.4.2 Chemical Composition Analysis

The chemical composition of the sample was studied by means of micro X-ray fluorescence (μ -XRF). For measuring, a M4 Tornado (Bruker Corporation) was used. Performing XRF, the sample is irradiated with an X-ray tube ($U = 50$ kV in this case) exciting atoms, which in turn emit characteristic X-rays, mainly from their inner shells. Afterwards, the intensity distribution of measured energy lines is related to the relative abundance of an element. Note, that elements of low atomic charge ($Z \lesssim 11$) cannot be detected due to the limited energy resolution of the measurement principle, since energy dispersive XRF was used [56]. Hence, niobium oxides expected on the sample surface are not visible.

The results of the XRF analysis are shown in table 7.2, the detection threshold of the measurement amounts to 0.01 % wt. The only significant impurity is 0.16 % wt. of calcium. Typical values for impurities of high-RRR niobium are below 10 $\mu\text{g/g}$ [57]. This is far below the resolution limit of this analysis (0.01 %wt. = 100 $\mu\text{g/g}$). Nevertheless no pollution with indium is found, therefore indium contamination of the sample surface can be excluded as the reason for the elevated R_S values. The impact of the pollution by calcium on R_S is still under investigation.

Element	wt. [%]
Nb	99.77
Ca	0.16
Fe	0.02
Ta	0.01
Cr	0.01
At	0.02

Table 7.2: Chemical composition found using XRF.

8 Summary and Outlook

The demanding requirements of today's applications of particle accelerators concerning cw operation at high gradients can only be met with SRF systems. In order to overcome the fundamental RF limits of niobium, research is ongoing identifying new materials suitable for SRF cavities. The concept of using thin films provides the availability of promising materials, e. g. Nb₃Sn. Producing thin multi-layer structures on a superconducting substrate, potentially overcomes the limits of the solid, boosting the performance of these materials even further.

The Quadrupole Resonator (QPR) is an ideal tool for RF characterization of superconducting samples. A wide parameter space of applied magnetic field, temperature and frequency is easily accessible, allowing the investigation of superconducting properties at operating conditions and rigorous comparison with theoretical models. Using a calorimetric RF-DC compensation method, the RF surface resistance is measured with high precision.

8.1 Design of an Optimized Calorimetry Chamber

In order to provide an easy mountable and exchangeable sample system, an optimized calorimetry chamber was developed. With the help of computer simulations, requirements towards the RF design of the new chamber were identified. The minimum height of the sample holder of 12 mm, as defined by measurement boundary conditions, is in agreement with RF requirements. This design provides thin samples, to be used for the systematic investigation of superconducting coatings and thin films, easily prepared in coating apparatuses.

Prototype tests revealed the necessity of a vacuum seal, which is implemented by using an indium wire gasket. Leak rate measurements yielded values below 10^{-10} mbar l/s, both at room temperature and under cryogenic conditions. The issue of an increasing leak rate during cool-down was solved by thermal cycling and retightening of fittings.

8.2 First RF Measurement

A first RF measurement with the optimized calorimetry chamber was performed using the QPR at CERN.

Measuring the resonant frequency of the QPR yielded a value of 1.35 mm for the gap between sample and quadrupole. From this the vertical offset due to both indium gaskets is derived to be 490 μm , which can be used in further measurements for vertical positioning.

The high values of RF surface resistance obtained are unexpected and show strong dependence on both, temperature and magnetic field strength. The increase of R_S near 3.4 K can be explained qualitatively by the surface resistance of indium. Approaching its critical temperature a sharply increasing surface resistance is expected from theory. The decrease of R_S for temperatures above T_c of indium as well as the rise of surface resistance with growing magnetic field strength require further investigations.

Measurements on the RRR resulted values higher than the one ordered for production of the calorimetry chamber (RRR=300), but with significant uncertainties. At high RRR, measurements using RF are limited in resolution in the superconducting as well in the normal conducting state. For measurements in the superconducting state a value of λ_0 close to λ_L results in big uncertainties on RRR since $\text{RRR} \propto \left[(\lambda_0/\lambda_L)^2 - 1 \right]^{-1}$. In the normal conducting state the anomalous skin effect becomes dominant, which only allows to set a lower boundary on RRR.

Using simulations concerning the thermal conductivity of the calorimetric system, a high value of RRR is confirmed.

After disassembly of the calorimetry chamber, stylus profilometry and X-ray fluorescence analysis were performed. Both measurements did not reveal any suspicious properties. The surface roughness obtained from profilometry is similar to the one, found at well performing SRF cavities treated with BCP. In the chemical composition, especially no pollution with indium was found, excluding indium contamination of the sample surface as the reason for the elevated R_S values.

8.3 Outlook

At the time of the RF measurement, only indium wires of diameter 0.5 and 1.0 mm were available. In order to obtain the vacuum tightness required for operation, the 1 mm wire was used and a circumferential gap between sample and tube was accepted. This may have had significant influence on the RF performance of the calorimetry chamber in a way that is not yet fully understood. Nevertheless, the results obtained are ambiguous and do not show the behavior, expected for dominant RF dissipation on an indium surface. Currently, indium wire of diameters 0.69 and 0.8 mm are available and presumably will provide a leak tight configuration without the circumferential gap. Therefore, further RF measurements are planned.

A Appendix

A.1 Picture of the Vacuum Test Environment

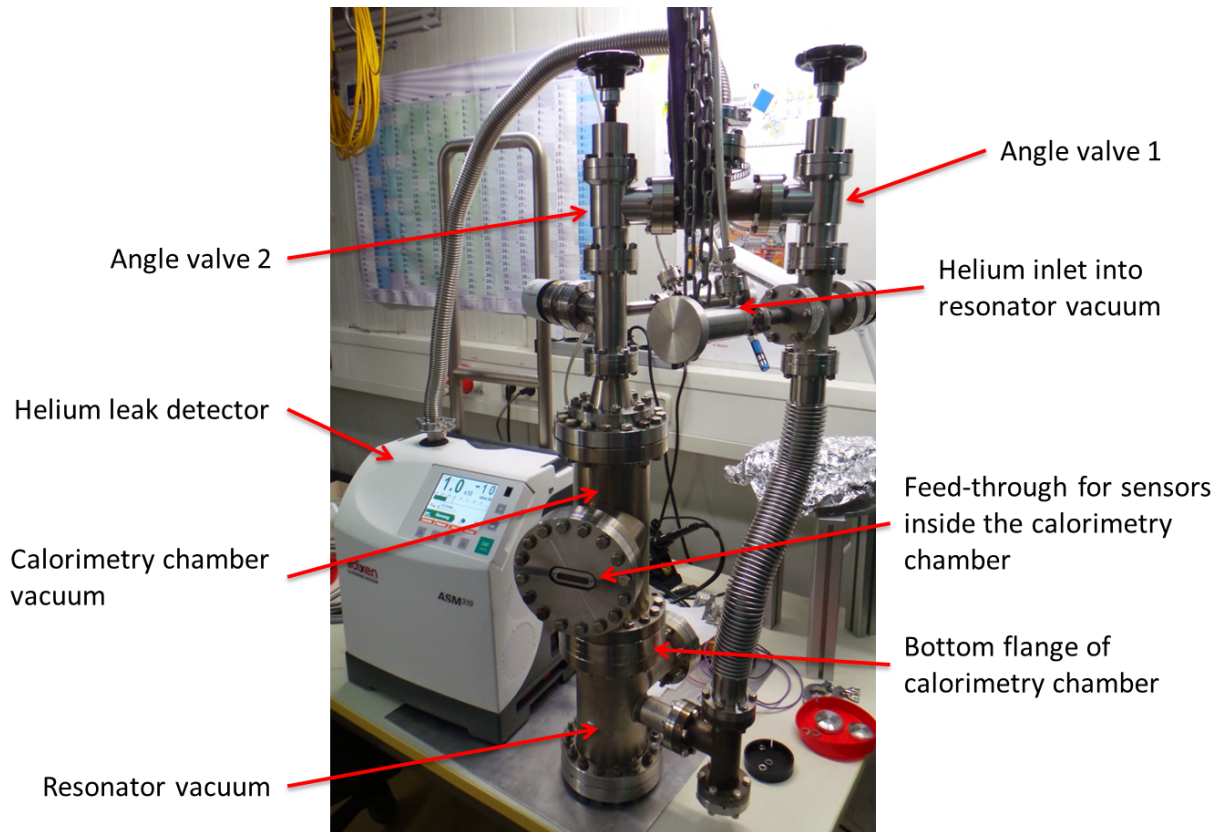


Figure A.1: *Picture of the vacuum test environment. The calorimetry is mounted upside down into the lower vacuum pipe (resonator vacuum).*

A.2 Pictures of Sample and Assembled Calorimetry Chamber

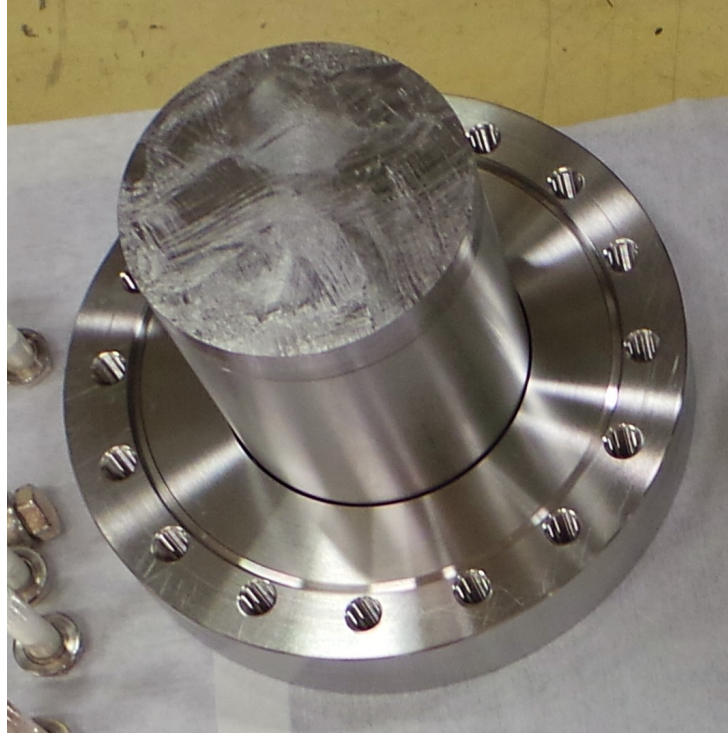


Figure A.2: *Assembled calorimetry chamber.*

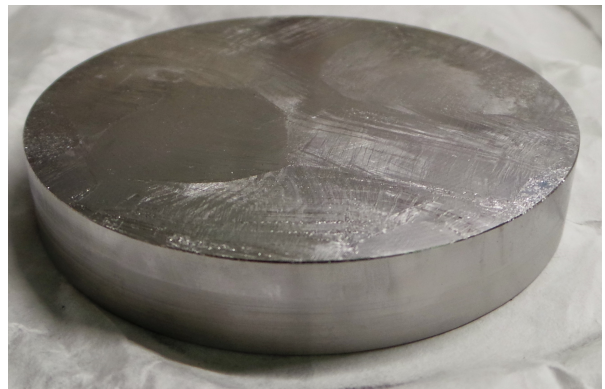


Figure A.3: *Niobium sample.*

Bibliography

- [1] H. K. Onnes. *Further experiments with liquid helium. C. On the change of electric resistance of pure metals at very low temperatures etc. IV. The resistance of pure mercury at helium temperatures.* Commun. Phys. Lab. Univ. Leiden 120b (1911), reprinted in: Proc. K. Ned. Akad. Wet. 13 II (1911) pp. 1274-1276.
- [2] H. K. Onnes. *Further Experiments with Liquid Helium. D. On the Change of the Electrical Resistance of Pure Metals at very low Temperatures, etc. V. The Disappearance of the resistance of mercury.* Comm. Leiden 122b (1911) in: Proc. KNAW 14 I (1911) pp. 113-115.
- [3] H. K. Onnes. *Further Experiments with Liquid Helium. G. On the Electrical Resistance of pure Metals, etc. VI. On the Sudden Change in the Rate at which the Resistance of Mercury Disappears.* Comm. Leiden 124c (1911) in: Proc. KNAW 14 II (1912) pp. 818-821.
- [4] H. K. Onnes. *Further experiments with liquid helium. J. The imitation of an Ampère molecular current or of a permanent magnet by means of a supra-conductor.* Comm. Leiden 140b and c (1914) in: Proc. KNAW 17 I (1914) pp. 12-20 and pp. 278-283.
- [5] H. K. Onnes. *Further experiments with liquid helium. L. The persistence of currents without electro-motive force in supra-conducting circuits.* Comm. Leiden 141b (1914) in: Proc. KNAW 17 II (1914) pp. 514-519.
- [6] F. London and H. London. *The Electromagnetic Equations of the Supraconductor.* Proc. R. Soc. Lond. A 149 (1935) 71.
- [7] V. L. Ginzburg and L. D. Landau. *On the Theory of Superconductivity.* Zh. Eksp. Teor. Fiz. 20 (1950) pp. 1064-1082, English Translation in: V. L. Ginzburg, On Superconductivity and Superfluidity, Springer-Verlag Berlin Heidelberg, 2009, pp. 113-137.
- [8] J. Bardeen, L. N. Cooper and J. R. Schrieffer. *Mircoscopic Theory of Superconductivity.* Phys. Rev. 106 (1957) 162.
- [9] J. Bardeen, L. N. Cooper and J. R. Schrieffer. *Theory of Superconductivity.* Phys. Rev. 108 (1957) 1175.
- [10] D. C. Mattis and J. Bardeen. *Theory of the Anomalous Skin Effect in Normal and Superconducting Metals.* Phys. Rev. 111 (1958) 412.
- [11] F. Caspers and M. Wendt. *RF Course.* Joint Universities Accelerator School, Archamps, France, 2015.

- [12] H. Padamsee, J. Knobloch and T. Hays. *RF Superconductivity for Accelerators*. Wiley, 2008. 2nd edition.
- [13] J. Knobloch and A. Neumann. *Introduction to Particle Accelerators*. Lecture at University of Siegen, 2011.
- [14] C. J. Gorter and H. Casimir. Phys. Z. 35 (963) 1934.
- [15] C. J. Gorter and H. Casimir. Z. Tech. Phys. 15 (539) 1934.
- [16] L. N. Cooper. *Bound Electron Pairs in a Degenerate Fermi Gas*. Phys. Rev. 104 (1956) 1189.
- [17] R. Casalbuoni. *Lecture on Superconductivity: Condensed Matter and QCD*. University of Florence, Italy, 2003.
- [18] G. Ciovati. *AC/RF Superconductivity*. arXiv:1501.07398v1, physics.acc-ph, 29 January 2015.
- [19] J. Knobloch. *SRF Systems for Particle Accelerators*. Lecture at University of Siegen, 2013.
- [20] J.-M. Vogt. *Magnetic Flux Trapping and Expulsion in Superconducting Niobium Cavities and Samples*. Humboldt University, Berlin and Helmholtz-Zentrum, Berlin, 2013.
- [21] J.-M. Vogt, O. Kugeler, J. Knobloch. *Impact of cool-down conditions at T_c on the superconducting rf quality factor*. Phys. Rev. Spec. Top. - Accel. Beams 16 (102002) 2013.
- [22] J.-M. Vogt, O. Kugeler, J. Knobloch. *High- Q operation of superconducting rf cavities: Potential impact of thermocurrents on the rf surface resistance*. Phys. Rev. Spec. Top. - Accel. Beams 18 (042001) 2015.
- [23] A. Gladun, C. Gladun, M. Knorn and H. Vinzelberg. *Investigation of the Heat Capacity of Niobium in the Temperature Range 0.05 – 23 K*. Journal of Low Temperature Physics 27 (1977) 873.
- [24] A. Gurevich. *Enhancement of rf breakdown field of superconductors by multilayer coating*. Appl. Phys. Lett. 88 (012511) 2006.
- [25] A. Gurevich. *Maximum screening fields of superconducting multilayer structures*. AIP Advances 5 (017112) 2015.
- [26] E. Brigant, E. Haebel. *Numerical Simulations in the Design of a Quadripolar Resonator*. Technical Note, EDMS 1178982, 1997.
- [27] E. Mahner, E. Calatroni, E. Chiaveri, E. Haebel and J. M. Tessier. *A new instrument to measure the surface resistance of superconducting samples at 400 MHz*. Rev. Sci. Instrum. 74 (2003) 3390.

-
- [28] E. Brigan, E. Haebel and E. Mahner. *The Quadrupole Resonator, Design Considerations and Layout of a New Instrument for the RF Characterization of Superconducting Samples*. Proceedings of the 6th European Particle Accelerator Conference, Stockholm, Sweden, 1998.
 - [29] E. Chiaveri, E. Haebel, E. Mahner and J. M. Tessier. *The Quadrupole Resonator, Construction, RF System, Field Calculations and First Applications*. Proceedings of the 6th European Particle Accelerator Conference, Stockholm, Sweden, 1998.
 - [30] T. Junginger, W. Weingarten and C. Welsch. *RF Characterization of Superconducting Samples*. Proceedings of the 14th International Workshop on RF Superconductivity, Berlin, Germany, 2009.
 - [31] T. Junginger, W. Weingarten and C. Welsch. *Review of RF Sample Test Equipment and Results*. Proceedings of the 15th International Workshop on RF Superconductivity, Chicago, Ill., USA, 2011.
 - [32] T. Junginger, W. Weingarten, C. Welsch and R. Seviour. *RF and Surface Properties of Superconducting Samples*. Proceedings of the 2nd International Particle Accelerator Conference, San Sebastian, Spain, 2011.
 - [33] R. Kleindienst, O. Kugeler and J. Knobloch. *Development of an Optimized Quadrupole Resonator at HZB*. Proceedings of the 16th International Conference on RF Superconductivity, Paris, France, 2013.
 - [34] T. Junginger. *Investigation of the Surface Resistance of Superconducting Materials*. Ruperto-Carola University of Heidelberg, 2012. Dissertation.
 - [35] T. Powers. *Theory and Practice of Cavity RF Test Systems*. Proceedings of the 12th International Workshop on RF Superconductivity, Ithaca, New York, USA, 2005.
 - [36] S. Aull, S. Doeber, T. Junginger and J. Knobloch. *High Resolution Surface Resistance Studies*. Proceedings of the 16th International Conference on RF Superconductivity, Paris, France, 2013.
 - [37] J. C. Slater. *Microwave Electronics*. Rev. Mod. Phys. 18 (1946) 441.
 - [38] L. C. Maier and J. C. Slater. *Field Strength Measurements in Resonant Cavities*. J. Appl. Phys. 23 (1952) 68.
 - [39] A. B. Pippard. *An Experimental and Theoretical Study of the Relation Between Magnetic Field and Current in a Superconductor*. Proc. Roy. Soc. London A216 (547) 1953.
 - [40] J. P. Turneure, J. Halbritter and H. A. Schwettman. *The Surface Impedance of Superconductors and Normal Conductors: The Mattis-Bardeen Theory*. Journal of Superconductivity 4 (341) 1991.

- [41] C. P. Poole, Jr., H. A. Farach, R. J. Creswick and R. Prozorov. *Superconductivity*. Academic Press, Elsevier Ltd., 2007.
- [42] D. M. Pozar. *Microwave Engineering*. John Wiley & Sons, Inc., 2005.
- [43] N. Marcuvitz. *Waveguide Handbook*. Dover Publications, Inc., 1951.
- [44] T. Kubo. *Analytical model of the magnetic field enhancement at pits on the surface of superconducting accelerating cavity*. arXiv:1307.5943v1, physics.acc-ph, 23 July 2013.
- [45] T. Kubo. *Models of the Magnetic Field Enhancement at Pits*. arXiv:1308.3311v2, physics.acc-ph, 7 October 2013.
- [46] V. Shemelin and H. Padamsee. *Magnetic Field Enhancements at Pits and Bumps on the Surface of Superconducting Cavities*. TTC-Report 2008-07, SRF 080903-04.
- [47] J. Knobloch, R. L. Geng, M. Liepe and H. Padamsee. *High-Field Q Slope in Superconducting Cavities Due to Magnetic Field Enhancements at Grain Boundaries*. Proceedings of the 9th International Workshop on RF Superconductivity, Santa Fe, NM, USA, 1999.
- [48] *COMSOL Multiphysics, Version 4.4.0.150*, www.comsol.de. accessed: 05.06.2015.
- [49] COMSOL. *RF Module User's Guide, Version 4.4*.
- [50] D. R. Lide, ed. *CRC Handbook of Chemistry and Physics*. CRC Press, Boca Raton, FL, 2005.
- [51] R. W. Shaw, D. E. Mapother and D. C. Hopkins. *Critical Field of Superconducting Tin, Indium and Tantalum*. Phys. Rev. 120 (1960) 88.
- [52] S. Aull, CERN. *Private Communication*.
- [53] F. Koechlin and B. Bonin. *Parametrization of the niobium thermal conductivity in the superconducting state*. Supercond. Sci. Technol. 9 (1996) 453.
- [54] National Institute of Standards and Technology, Cryogenic Technologies Group. *Thermal Conductivity of 316 Stainless Steel*. http://www.cryogenics.nist.gov/MPropsMAY/316Stainless/316Stainless_rev.htm. accessed: 05.06.2015.
- [55] O. S. Romanenko. *Surface Characterization of Nb Cavity Sections - Understanding the High Field Q-Slope*. Cornell University, 2009. Dissertation.
- [56] B. Beckhoff et. al. *Practical X-Ray Fluorescence Analysis*. Springer, 2006.
- [57] W. Singer. *SRF Cavity Fabrication and Materials*. arXiv:1501.07142v1, physics.acc-ph, 18 January 2015.

Danksagung

Diese Arbeit wäre nicht ohne die Hilfe und Unterstützung Vieler möglich gewesen. Ich möchte daher an dieser Stelle die Gelegenheit wahrnehmen und mich bei all denen bedanken, die mich während der Zeit meiner Masterarbeit – vor und/oder hinter den Kulissen – unterstützt haben.

Besonderer Dank gilt zuerst Herrn Prof. Dr. Jens Knobloch für die Möglichkeit, diese Arbeit in seiner Arbeitsgruppe durchführen zu können und Herrn Prof. Dr. Andreas Jankowiak für die Bereitschaft, sich als Zweitgutachter zur Verfügung zu stellen.

Dr. Oliver Kugeler und Raphael Kleindienst gilt großer Dank für die Betreuung, Hilfe und ständige Ansprechbarkeit während meiner Arbeit. Außerdem möchte ich mich für wertvolle und schnelle Korrekturvorschläge bedanken, die das Zusammenschreiben ungemein bereicherten.

Die Messungen mit dem Quadrupolresonator am CERN wären ohne die großzügige Hilfsbereitschaft von Sarah Aull nicht möglich gewesen. Ich bedanke mich außerdem für die große Geduld beim Beantworten vieler Emails und die Gelegenheit, das berühmte Schweizer Käsefondue kennen zu lernen.

Ein Dank für schnelle und unkomplizierte Hilfe bei Tests und Messungen am HZB geht an Sascha Klauke und Michael Schuster. Gerade bei Messungen mit flüssigem Stickstoff und in Fragen der Vakuumtechnik standen sie mit helfenden Hände und Ideen stets zur Verfügung.

Abschließend gilt ein herzlicher Dank den Kolleginnen und Kollegen in den Instituten FG-ISRF und FG-IA für das freundliche Miteinander und die gute Zusammenarbeit. Hier sind besonders Eva, Jens, Julia, Martin, Stephi, Tom und natürlich Claudia zu nennen, ohne die die vielen Stunden im Büro nicht so schön gewesen wären. Ein besonderer Dank geht außerdem an Pia und meine Familie, die mir außerhalb des HZB immer zur Seite standen.

Herzlichen Dank!

Erklärung

Hiermit erkläre ich, dass ich die vorliegende Masterarbeit selbstständig verfasst und keine anderen als die angegebenen Quellen und Hilfsmittel benutzt sowie Zitate und Ergebnisse anderer kenntlich gemacht habe.

Berlin, den

SEBASTIAN KECKERT